UNIVERSITÀ DI PISA

Facoltà di Scienze Matematiche, Fisiche e Naturali
Corso di Laurea Specialistica in Scienze Fisiche

Tesi di Laurea Specialistica

Ab initio study of crystalline Polymer Solar Cells

Relatori:
Prof. Renato Colle
Prof. Giuseppe Grosso

Candidato:
Alberto Ronzani

Anno Accademico 2009-2010

Abstract

Poly-(3 hexylthiophene) (P3HT) and phenyl-C_{61}-butyric acid methyl ester (PCBM) are two widely used constituents in the bulk heterojunction of polymer photovoltaic cells, where their crystalline domains fulfill the role of electron donors and acceptors, respectively.

By means of an *ab initio* approach via numeric quantum mechanical computations in the framework of Density Functional Theory, the crystalline morphology of such domains has been fully ascertained, and several experimentally observed physical properties have been successfully reproduced.

Acknowledgements

We acknowledge the allocation of computer resources from INFM *Progetto Calcolo Parallelo* 2007, and the MURST-PRIN 2006 *Meccanica Quantistica Molecolare: Metodi ed Analisi di Nuovi Fenomeni*.

Contents

Introduction

Many energy sources on Earth originate from the Sun. Either bio-fuels or weather-related sources like hydroelectric or wind power generators are ultimately powered by solar irradiation. Fossil fuels themselves can be thought as solar energy stored in chemical form which allows for a cheap conversion to electric energy. At the time of writing, most of the worldwide energy consumption is obtained by combustion of fossil fuels. The prospect of the exhaustion of fossil reserves, as well as the evaluation of the costs of the environmental effects due to the massive release of carbon dioxide and other polluting byproducts of combustion of fossil fuels have began to stir some interest in the development of energy sources which are either renewable and more environmentally-friendly.

Photovoltaics exploit the abundance of solar radiation throughout the world as well as the versatility of electricity as a means to distribute energy, providing a method for the direct conversion of the energy of solar photons into the energy associated with a direct electrical current. The typical limiting factor in the adoption of photovoltaics as an energy source is its cost. The majority of commercial modules makes use of the photovoltaic effect in crystalline or poly-crystalline silicon junctions, whose manufacturing costs are high; typically, in a silicon-based photovoltaic installation, the cost of the modules alone can add up to 80% of the total. In response to this problem other materials are being devised as substitutes for the expensive crystalline silicon.

Polymer solar cells (PSCs) use blends of conducting polymers as photovoltaic absorbers. The synthesis as well as the processing of thin films of conducting polymers is significantly cheaper than crystalline silicon manufacture. Most conducting polymers behave as direct gap semiconductors, although their band gap is generally wider than common inorganic semiconductors. PSCs feature large absorption coefficient for visible light, which results in a significant boost to the power conversion efficiency. On the other hand, conducting polymers have much lower charge carrier mobility than their inorganic counterparts. Overall, the efficiency of an organic solar cell is still low compared to silicon based cells.

It is expected that this gap will be reduced in the future, thus enabling the use of organic solar cells as a viable alternative to the expensive silicon modules.

The means to achieve such a goal include arranging the bulk of the cell in order to maximize the interfacing surface of the acceptor and donor domains. It is known that the crystallization process of both P3HT and PCBM, two common choices as donor and acceptor material in organic solar cells, is not as straightforward as in inorganic semiconductors, particularly in thin film processing. It is not easy to grow crystallites with the desired size and orientation, much less arranging them in order to maximize the surface of the junctions .

Our work aims to determine from first principles the crystalline morphology of P3HT and PCBM domains. Structural, optical and electronical properties have been simulated and compared for consistency to actual measurements present in current literature. We believe that the detailed knowledge of crystalline morphology of the components of polymer solar cells is beneficial to the understanding and to the control of the crystallization processes, and ultimately to the realization of high efficiency devices.

The contents of this thesis can be outlined as follows:

- Chapter 1: enumeration and description of photovoltaic (PV) technologies, underlying physical principles, and real world use cases.
- Chapter 2: analysis of P3HT domains.
- Chapter 3: analysis of PCBM domains.
- Appendix A: technical reference of the numerical methods used throughout the thesis.

Chapter 1

Photovoltaics

1.1 General principles

1.1.1 Historical introduction

Photovoltaic technologies consist in devices which are able to provide a source of electric current under the influence of light. The conversion between the energy of a photon and the electrical potential energy of a charge carrier is termed "photovoltaic effect". This definition clearly encompasses a wide variety of physical phenomena. As an introduction to the chapter, a brief historical review of photovoltaic devices is presented. More details about the historical development of photovoltaics can be found in [1].

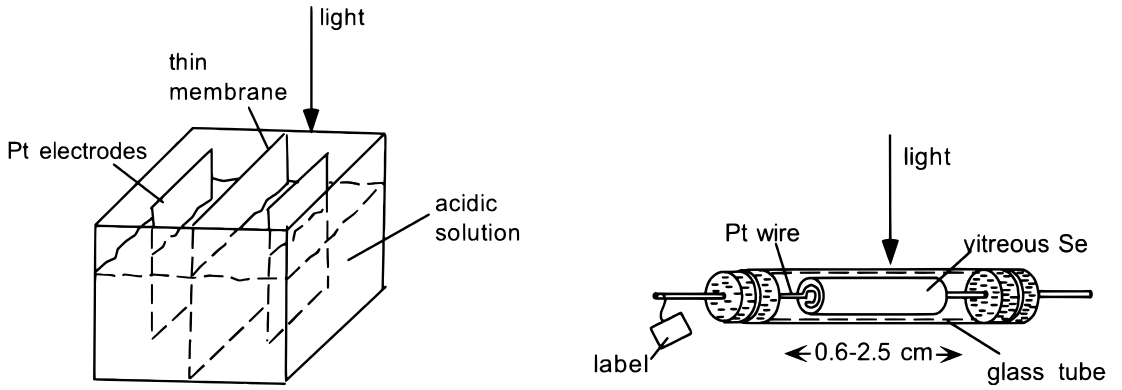

(a) Becquerel [2, 3]: electrolytic cell based on photovoltaic effect in a solution of Ag salts.

(b) Adams and Day [4]: solid state cell based on photovoltaic effect in Pt/Se contacts.

Figure 1.1. Early photovoltaic devices; pictures reproduced from [5].

The first account [2, 3] of a photovoltaic effect is due to Edmond Becquerel, who in 1839 observed the onset of an electrolytic current upon shining blue light on electrodes made of platinum coated with silver salts when dipped in an acidic bath (fig. 1.1(a)). The first demonstration of a solid state photovoltaic effect happened in 1876, when Adams and Day ascertained that it was possible to start an electric current by shining light on selenium specimens [4] (fig. 1.1(b)). Their work eventually led to the first thin-film selenium-based solar cells being fabricated by Fritts in 1883. Following development involved the use of cuprous oxide and thallous sulphide as the absorbing layer (ca. 1930). The earliest realization of a silicon p-n junction photovoltaic device is due to Russel Ohl, who exploited photovoltaic effect on semiconductor junctions that he found to accidentally occur in the processing of pure silicon ingots. Slates cut from those ingots (fig. 1.2) showed good rectifying properties and a high thermoelectric coefficient, acting as crude diodes. In 1948, well before the understanding of the role of impurities in crystalline silicon, Ohl

patented [6] the first p-n silicon solar cells. The development of crystal growth techniques allowed for more efficient designs of the junction, so that, in 1954, Pearson, Fuller and Chapin [7] were able to reach a record efficiency of 6%.

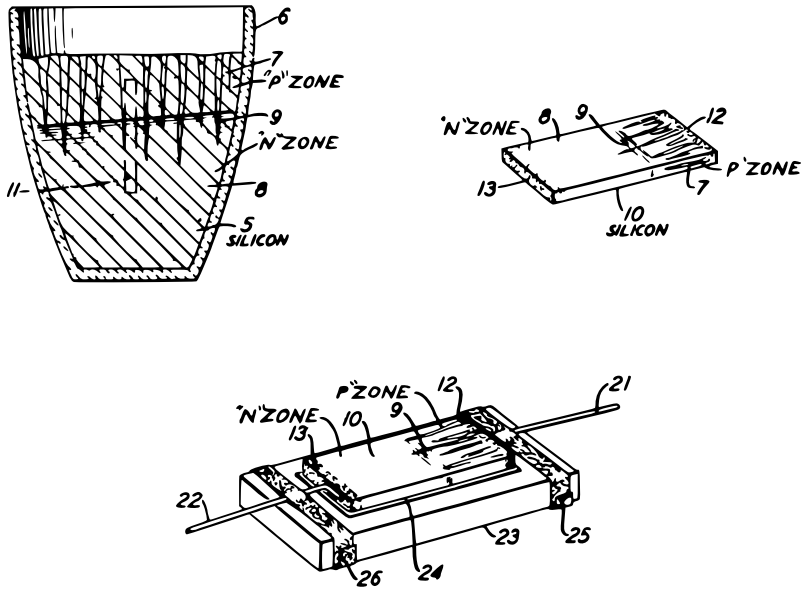

Figure 1.2. Sketches detailing cell preparation from Ohl's patent [6]. After the crystallization of silicon two different solid phases may be present: a "p" phase rich in crystalline pillars (marked as 7), and a "n" phase (marked as 8) whose morphology is more uniform. A p-n junction (marked as 9) appears as a barrier between the two phases. A slice of silicon is cut from the ingot to include the p-n junction, and electrodes (21,22) are attached to each phase. The resulting device acts as a crude diode in which the photovoltaic effect can be observed.

By the late 1970s the efficiency of silicon junction-based solar cells could benefit from sophisticated doping techniques, adapted from microelectronic device manufacture. Gradually, it became evident that the indirect band-gap of silicon was a limiting factor in the efficiency of the absorption of light. The adoption of various III-V compounds and alloys, as well as the stacking of multiple junctions gave a significant boost to the efficiency of photovoltaic cells.

Band-gap engineering concepts play a major role in modern efficient photovoltaic solar cells. At the time of writing, the best performing cells (featuring over 40% efficiency under concentrated radiation) are based on III-V heterostructures in multijunctions [8]. On the other hand, as noted in the Introduction, current research has expanded its focus from efficiency to cost-effectiveness, so that a wide range of implementations is being tested. The actual physical phenomena which realize the photovoltaic effect in a particular device are dependent on the implementation. A

simple review of the general characteristics of physical photovoltaic systems is given in the following subsection.

1.1.2 Functional structure of a photovoltaic device

A photovoltaic device converts the energy of incoming photons into potential electrical energy of charges which are collected into electrodes. This process can be schematically split into three steps:

1. Quantum excitation induced by light absorption or scattering

2. Generation of "free" charge carriers from the excited states

3. Selective transport of carriers up to the relevant electrode

These steps may or may not be spatially resolved in a particular device, yet this conceptual framework is useful both to understand the operation and to minimize the energy loss channels of a given solar cell type.

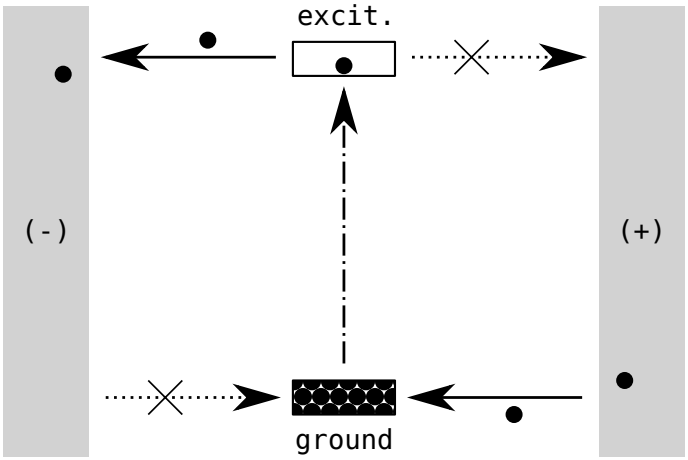

Figure 1.3. Schematic functional diagram of a photovoltaic device: An electrical potential difference between two electrodes is obtained by establishing a flux of charge carriers, electrons in this case (represented by black dots). This flux is driven by photoinduced excitation of quantum systems leading to the generation of "free" conduction electrons. Selective transport properties allow the efficient removal of electrons from excited states to the negative electrode, while replenishing the ground states with electrons migrating from the positive electrode. Loss channels are marked with crossed arrows.

The role of the first step is almost obvious; it is clear that no energy conversion whatsoever is possible without interacting with the electromagnetic field. This interaction must result in quantum transitions of appropriate absorbers[1] whose transition energies should closely match the available energy spectrum of solar photons. The second step is actually granted by one-electron transitions themselves in crystalline silicon cells. However, a specific mechanism to unbind the charge carriers may be required in other cases. The latter step is also not to be overlooked: carrier transport should be efficient to maintain optimal transition rates, as well as selective to ensure that each carrier reaches the electrode appropriate to the sign of its charge.

1.1.3 Electrical modeling of a photovoltaic source

The electrical properties of a photovoltaic source depend on the physical processes occurring in that particular solar cell: these processes have been subjected to thorough analysis [9]. In general, however, the behavior of a photovoltaic source can be approximately modeled in terms of basic circuit elements[2]. In fig. 1.4 is reported a typical equivalent circuit diagram for the analysis of photovoltaic sources.

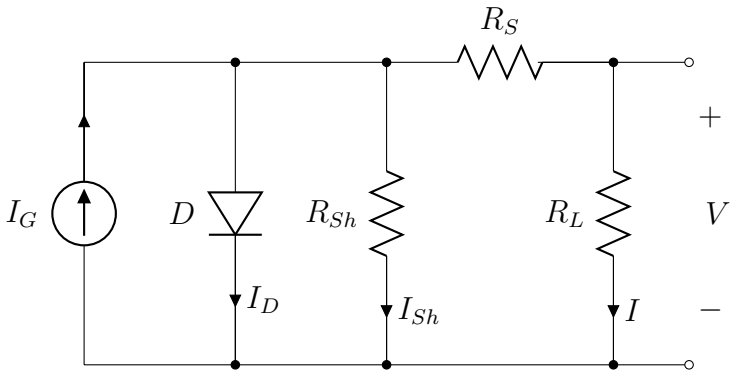

Figure 1.4. Electrical model of a photovoltaic device. The photovoltaic effect supplies a constant flux of carriers (I_G), while charge selective transport in the cell is modeled with a rectifying diode (D). Recombination losses are represented by a shunt resistor (R_{Sh}), while finite mobility of carriers as well as non ideal electrodes are included as the effect of a series resistor (R_S). The circuit is completed with an external load (R_L).

The analysis of this circuit provides a starting point for understanding the current-voltage characteristics of most photovoltaic cells, and it is useful to define

[1] One-electron states in crystals, electronic states in dye molecules, quantum dots or impurities, collective quantum excitations like plasmons or excitons, to name a few.

[2] See for example the use made in [10].

some widely used efficiency-related concepts. From the equivalent circuit diagram it is straightforward to derive the current-voltage characteristic equation. The whole circuit (both source and load) is described by the following system of equations:

$$\begin{aligned} V &= IR_L \\ I = I_G - I_{Sh} - I_D &= I_G - \frac{V + IR_S}{R_{Sh}} - I_0 \left(\exp\left(e\frac{V + IR_S}{k_B T} \right) - 1 \right) \end{aligned} \tag{1.1}$$

This system features two independent equations for the two unknowns I and V, thus the choice of R_L uniquely determines the values of I and V, as expected. It is reasonable to choose the load in order to maximize the electrical power extracted from the source. The optimal work point numerical estimation is displayed in fig. 1.5.

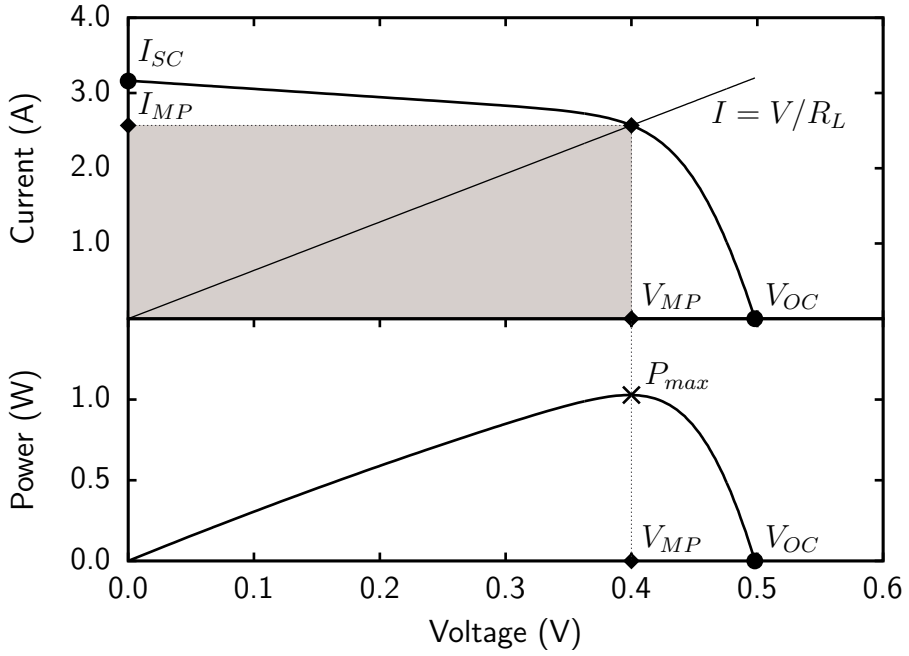

Figure 1.5. Current and power characteristics obtained from numerical solution of eqn. 1.1 are plotted against a common voltage axis. The current-voltage characteristic of the ohmic load with optimal R_L intersects the characteristic of the source at the voltage of maximum power (V_{MP}). The shaded area in the topmost graph equals $P_{max} \equiv V_{MP} I_{MP}$.

Efficiency-related concepts

Fill Factor

The fill factor (FF) is defined as the ratio between the actual maximum power that can be extracted from the cell and the upper limit $P_{lim} = V_{OC} I_{SC}$, where I_{SC} is the short circuit current and V_{OC} is the open circuit voltage.

$$FF \equiv \frac{P_{max}}{P_{lim}} = \frac{V_{MP} I_{MP}}{V_{OC} I_{SC}} \tag{1.2}$$

Typically, FF values lie between 0.25 (cell dominated by the shunt resistor behavior) and 1.0 (characteristic with ideal step-like shape).

Photoresponsivity

An important property for a photovoltaic source is the dependency of the electrical output from the incident light spectrum. The photoresponsivity (PR) is defined as the ratio between the photocurrent produced under short circuit (I_{SC}) and the power of the light source per fixed wavelength.

$$PR(\lambda) = \frac{I_{SC}(\lambda)}{P_{inc}(\lambda)} \tag{1.3}$$

The photoresponsivity is measured by monochromatic radiation, thus it is independent on the emissive spectrum shape of the actual light source, although, in principle, it can be dependent on the intensity of the incident radiation[3].

External Quantum Efficiency

A related quantity is the external quantum efficiency (EQE), defined as the ratio between the number of extracted charges and the number of incident photons at a given wavelength.

$$EQE(\lambda) = \frac{N_e}{N_{ph}(\lambda)} \tag{1.4}$$

Naturally, photoresponsivity (PR) can be derived from external quantum efficiency (EQE) as follows:

$$PR(\lambda) = \frac{e}{h\nu} EQE(\lambda) = \frac{e\lambda}{hc} EQE(\lambda) \tag{1.5}$$

Power Conversion Efficiency

The power conversion efficiency (PCE) is defined as the ratio between the

[3]This dependence can be caused by saturation phenomena in the excited states of the quantum absorbers, for example.

electrical power output and the incident optical power (P_{inc}), integrated over the whole spectrum of the source.

$$PCE = \eta = \frac{P_{max}}{P_{inc}} = FF\frac{V_{OC}I_{SC}}{P_{inc}} \tag{1.6}$$

As a result of the integration of the incident spectrum, the value of PCE is dependent on the particular light source used in the measurement. For the sake of reproducibility of PCE measurements, standard irradiance spectra have been defined and implemented in "solar simulators".

1.2 Modern implementations

This section a concise review of modern photovoltaic technology is presented. Selected works that fully develop this subject include [11, 12].

1.2.1 Absorbing materials

The central feature of photovoltaic devices consists in an excitable quantum mechanical system able to absorb energy from solar radiation. Several materials have been conceived to fulfill this goal (sources for efficiency data are [11, 13]):

Crystalline Silicon
The majority of currently installed photovoltaic devices uses mono or polycrystalline silicon as the absorbing layer. Crystalline silicon is an indirect band-gap semiconductor with an energy gap of 1.1 eV, which results in an absorption onset at $\simeq$1100 nm, providing a fair match with the available solar spectrum. On the other hand, the indirect gap causes relative poor values for the absorption coefficient, so that thick cells are required to fully collect incoming solar radiation. Transport selectivity is obtained by doping silicon to form p-n junctions. Silicon is a readily available non-toxic material, however the processing required to obtain suitable high quality crystals is neither cheap nor environmentally friendly for what concerns carbon emissions. Typical efficiencies figures for cells are 25% in lab and 16–20% in commercial modules.

Amorphous Silicon (a-Si)
Amorphous silicon consists in an alloy of silicon and hydrogen atoms, whose inclusion hampers the long range lattice order of silicon. Lattice disorder correlates to changes in the optoelectronic response of the medium. The optical gap increases from 1.1 to 1.7 eV, actually resulting in a better match for the solar spectrum than the crystalline counterpart. However, recombination sites

induced by disorder cause the carrier mobility in a-Si to be quite low, so that charge separation and collection has to be supported by superimposed electric field. Amorphous silicon also suffers from light-induced performance degradation which can be as high as 20% of the power conversion efficiency. The absorption coefficient is higher than for crystalline silicon, allowing the manufacture of thin films, whose processing is cheap and fast. Typical cell efficiencies are 10% in lab and 6–8% in commercial modules.

Copper Indium Gallium Diselenide

Copper indium diselenide (CIS) and copper gallium diselenide (CGS) are direct band-gap ternary semiconductors with energy gaps of 1.1 and 1.7 eV, respectively. CIGS defines the alloy $CuIn_xGa_{1-x}Se_2$, whose energy gap can be adjusted by varying the relative proportion between indium and gallium. The copper indium gallium diselenide (CIGS) layer acts as p-type semiconductor, while another n-type semiconductor is needed to form an effective p-n junction. A common choice is a layer of n-doped cadmium sulphide. The direct band gap in CI(G)S induces high absorption coefficients, allowing the use in thin films applications. Overall stability and efficiency figures are good, with the best lab cells at 20%, while commercial modules score 13–17%. The main drawback for CI(G)S based solar cells is the necessity of using rare or polluting elements in the actual cells, which leads to rather high costs in the manufacturing as well as in the decommissioning processes.

Cadmium Telluride

Cadmium telluride shows a direct band gap at 1.45 eV, which is close to the optimal for absorbing solar spectrum with a single junction. A CdTe solar cell is similar to a CIGS solar cell in structure, featuring a layer of CdS as n-type acceptor and CdTe as p-type donor. The production costs benefit from a simple process, and, given that tellurium is more available than indium, manufacturing is cheaper than CIGS solar cells. Efficiency figures are similar, with the best lab cells at 17% and commercial modules scoring 11%. As in the CIGS case, the presence of cadmium raises considerable environmental alertness, even though CdTe is thought to be a rather stable compound.

Gallium Arsenide multi-junction

Gallium Arsenide is a semiconductor with an optimal direct band gap of 1.42 eV. Its main photovoltaic application is in spacecraft solar cells. Their use is justified by the fact that in space applications the leading costs are weight related and GaAs multi-junction devices currently offer the best watt-peak per kg ratio among all photovoltaic devices. Since 1980s researchers have been able to manufacture efficient lightweight thin films by growing multiple junctions, each engineered to absorb a specific part of the available solar spectrum.

A typical spacecraft solar cell is composed of three junctions: a top layer of gallium indium phosphide able to absorb blue or ultraviolet (UV) photons, a middle layer of gallium arsenide for the red spectrum, and a final layer of germanium which is suited for infrared (IR) absorption, having an energy gap of 0.7 eV. Such devices score efficiencies as high as 32%, outperforming all other photovoltaic technologies, the drawback being the production costs.

Organic Dyes

The strong optical properties of some biological pigments have been exploited since stone age in the manufacture of colorants. Light absorption occurs due to transitions between ground and excited electronic states in the molecule. In contrast to the case of inorganic semiconductor-based devices, light absorption in a molecule does not readily result in the generation of free carriers, due to the fact that the ionization energy is usually much higher than the energy of a visible photon. However, in 1991 Grätzel and O'Regan discovered that if excited dye molecules were in contact with a layer of titanium dioxide, the photo-excited electronic molecular states could make transition to free electrons in the conduction band of TiO_2, leaving behind an oxidized molecule. For the electron the diffusion in titania is a faster process than the recombination with the dye molecule, so that it can be extracted from an electrode attached to TiO_2. The positive counter-electrode is dipped in an electrolytic bath, providing charge replenishing for the ground state of the dye molecules. A Grätzel cell has typical efficiency of 10% [14], its manufacturing process is very cheap, and does not involve toxic compounds. However, the necessity for a liquid electrolyte is limiting both to the speed of the manufacturing process and to the stability of the devices when exposed to the temperature range typical of outdoor environment.

1.2.2 Optics

In addition to the engineering of efficient light absorbing mechanisms, photovoltaic solar cells can also benefit from optical conditioning of incoming radiation. Depending on the implementation details, the yield of a photovoltaic energy source can be enhanced by the following means:

Orientation

Photovoltaic array modules perform better when placed in full sunlight. Ideally, the array should be oriented and tilted from the horizontal plane so that solar radiation is normal to the cells at noon. It is obvious that for a fixed installation this condition cannot be valid throughout the whole year. A rule of thumb for the tilt is given by the latitude of the site of the installation, so

that the array modules are normal to noon sun rays during equinoxes. This tilt should then be adjusted taking into account the contingent insolation properties of the site (weather and permanent shadows) in order to maximize the energy produced during the whole year.

Concentration and Tracking

Lenses or mirrors can be used to increase the light intensity at the surface of the cell. Low concentration fixed setups are useful to convey light uniformly during a day, while high concentration mirrors or lenses paired with active sun tracking devices allow to use fewer cells per given power output. The latter solution goes under the name of concentrating photovoltaics (CPV) and aims to reduce the cost of a photovoltaic installation by minimizing the volume of absorbing material needed, the drawback being the setup and maintenance cost of the tracking mechanisms.

Light Trapping

Most photovoltaic cells are equipped with a metallic sheet which serves both as a reflecting layer and as electrode. The external face of the cell can be textured to force an incoming light ray to bounce back and forth in the absorbing bulk, thus reducing the cell reflectivity and increasing the density of photons available for absorption.

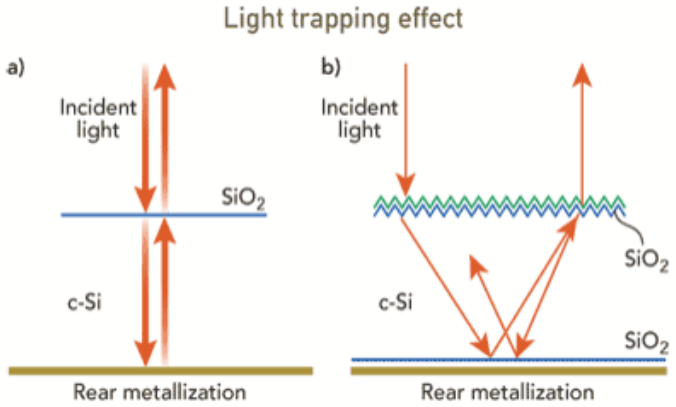

Figure 1.6. Light trapping effect in a crystalline silicon cell. Incoming photons are forced to bounce back and forth between the rear metallization and the textured surface of the absorbing layer. Reproduced from [11].

1.3 Polymer Solar Cells

Organic solar cells (OSCs) consist in devices in which the photovoltaic effect is realized via organic molecules or compounds. In section 1.2.1 organic dyes were mentioned as a type of photoexcitable absorber for Grätzel cells, whereas in the present section we focus on the working principles of PSCs, which are based on conducting polymers. Since the discovery of high conductivity in iodine-doped poly-acetylene (which earned Heeger, MacDiarmid and Shirakawa the 2000 Nobel Prize in Chemistry), the field of conducting polymers has been flourishing with research and commercial applications, given the unique processability properties related to their solubility. Functionalization by side-chains allows conducting polymers to be readily dissolved in common solvents to be used as ink, enabling localized deposition as well as efficient large area batch production.

1.3.1 Conjugated systems

All of the known conducting polymers share a common structural feature: a backbone containing a conjugated bond sequence, *i.e.* an alternating pattern of single and double bonds. Poly-acetylene (PAT), a typical conjugated polymer, features a backbone of sp^2 hybridized carbon centers, each of which contributes a p_z valence electron. In informal terms, the π bonds form a highly delocalized molecular orbital whose excited states can be populated with excess charges obtained upon doping or photoexcitation. These charges can then move with significant mobility, hence the conducting properties.

(a) PAT (b) PPV

Figure 1.7. Examples of conjugated polymers.

More precisely, an infinitely long crystalline polymer has a discrete translational symmetry along its backbone axis, so that k-space analysis is applicable. The resulting energy band structure is akin to that of an inorganic semiconductor, showing valence as well as conduction bands related to the highest occupied and lowest unoccupied electronic states, respectively. In fact, non k-space treatments directly refer to the conduction and valence bands respectively as the lowest unoccupied molecular orbital (LUMO) and highest occupied molecular orbital (HOMO) of finite

macromolecules. In conjugated polymers, the conduction and valence band states are typically due to weakly bound electronic states in shallow π-type orbitals, deriving either from linear combinations of p_z atomic orbitals (such is the case of PAT), or from more complex systems involving phenyl groups (see fig. 1.7).

1.3.2 Cell architecture

A typical polymer solar cell is a thin film device based on a light-absorbing bulk sandwiched between two electrodes. Glass or plastic substrates coated with indium tin oxide (ITO) are a usual choice for the transparent electrode, while a reflective layer of metal is commonly used as the back electrode. The optical transitions in the light-absorbing bulk result in excited electronic states made of electron-hole bound pairs called *excitons* whose binding energy can be considerable (0.1–1 eV); this directly results in the lowering of the absorption onset in comparison with the single-electron photoexcitation process typical of inorganic semiconductors. The exciton is localized and its lifetime allows for diffusion up to distances of 20 nm, when it recombines either radiatively or non-radiatively. For photovoltaic effect to be possible, the exciton must be broken into free electron and hole within the lifetime of the excited state. Each carrier must then selectively diffuse towards the electrode of relevance, depending on the sign of the charge. This goal can be realized in different ways, each of which requires a particular architecture for the bulk of the PSC.

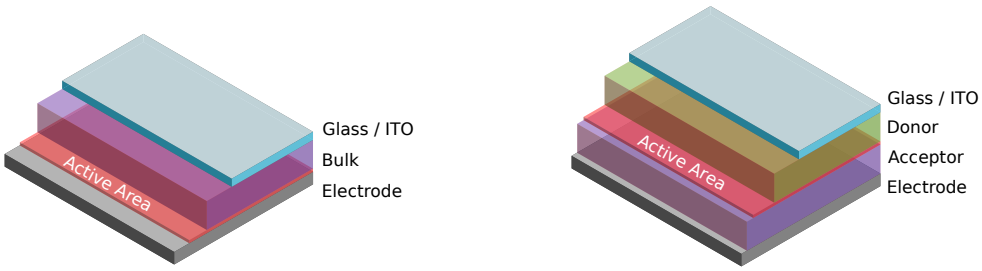

(a) Monolayer PSC (b) Bilayer PSC

Figure 1.8. Layered architectures.

In the simplest case (single layer PSCs), the excitons are broken down by the Schottky electrical field near the junction between the absorbing bulk and one of the electrodes. The resulting architecture is simple, but the drawback of this setup is that photoabsorption events directly resulting in production of free charges occur only within a thin layer near the Schottky contact, shown as the red "active area" in

figure 1.8(a). In a bilayer PSC, the exciton breaking mechanism is obtained by pairing the donor domain of the polymer with a suitable electron acceptor, which also provides the benefit of improved transport selectivity. Typical donor-type (fig. 1.9) polymers are P3HT and MDMO-PPV, while commonly used acceptors (fig. 1.10) include PCBM and CN-MEH-PPV.

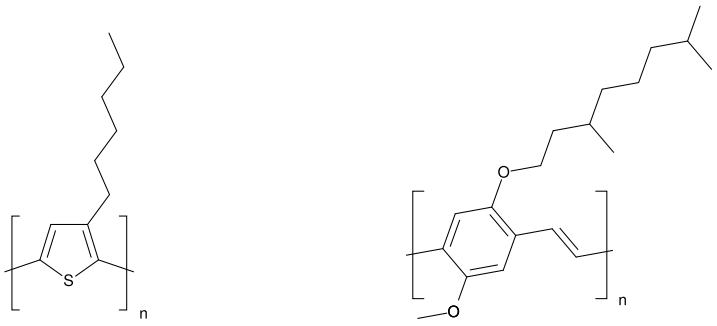

(a) P3HT (b) MDMO-PPV

Figure 1.9. Commonly used donor polymers

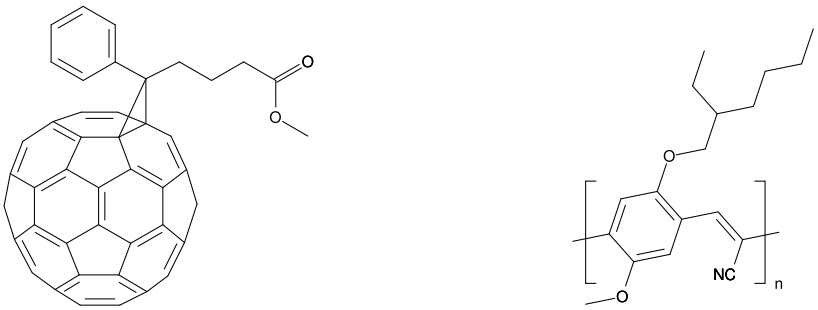

(a) PCBM (b) CN-MEH-PPV

Figure 1.10. Commonly used acceptor polymers

The juxtaposition of donor and acceptor domains causes the onset of a strong potential gradient, which is able to break up the excitons by drawing the electron into the n-type acceptor (figure 1.11).

After the dissociation of the exciton, the carriers drift towards the extraction electrode possibly assisted by the electric field arising from the different work function values for the electrodes. With a recombination lifetime of $\tau \approx 1\ \mu$s, the typical drift length is $d \approx 100$ nm, a figure which also represents an estimate for the order of magnitude of thin film thickness required for an efficient PSC.

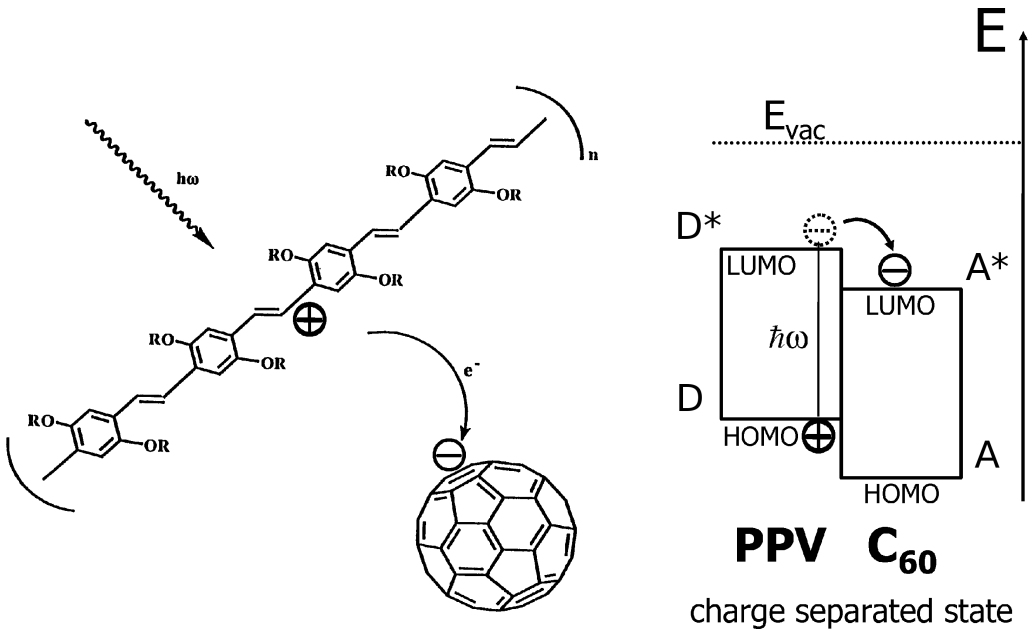

Figure 1.11. Photoinduced charge transfer. This phenomenon can be envisioned as a transition between the excited state of the donor (D*) and the excited state of the acceptor (A*). If this transition is faster than the recombination (D* - D) and backtransfer (A* - D) lifetimes, the charge separated state is metastable. Reproduced from [15].

1.3.3 Outlook

From the previous arguments it should be evident that even in bilayer architectures (figure 1.8(b)) just a thin slice of the active bulk actually contributes to photocurrent generation, the limiting factor being the small exciton diffusion length. The PCE of bilayer PSCs has been improved with the introduction of the concept of bulk heterojunctions (BHJs), in which the interface area between donor and acceptor is increased by interpenetrating their domains in the whole bulk volume of the absorbing layer. Thin films obtained by the casting and subsequent annealing of a liquid blend of donor and acceptor constituents generally present a disordered arrangement of semi-crystalline domains as shown in figure 1.12(a).

Ideally, the interpenetrating domains should have a width comparable with the exciton diffusion length and should be connected to their relevant electrode within the diffusion length of the charge carriers. This ideal setup is represented in figure 1.12(b). The realization of an ordered bulk heterojunction depends on the growth of crystallites of controlled shape and orientation. To this day, research has been attempting to control those parameters by acting on annealing procedures, doping, or otherwise changing the regiochemical characterization of the constituent

(a) Disordered BHJ (b) Ordered BHJ

Figure 1.12. Bulk heterojunction schematics

donor or acceptor samples. Significant effort has also been spent for investigating the dependence of optical and electronic properties on such processing details.

The best performing polymer-fullerene solar cells feature more than 6% in-lab power conversion efficiency (2009) [16]. Since this field of study is rather new, there is no reason to believe that higher yields are not available. One major advantage of organic solar cells is that the synthesis of polymers as well as their processing is much cheaper than inorganic semiconductor technologies. This makes polymer solar cells a strong candidate for a low-cost photovoltaic energy source. The micromorphology of the crystalline packing of donors and acceptors is critical both to their optoelectronic properties and to the kinetics of crystallization. The present thesis focuses on the *ab initio* determination of the structural and electro-optical properties of P3HT and PCBM, whose crystalline packing structures have been so far elusive. We believe that our results can be beneficial both to the understanding of the observed physical properties and to suggest novel ways to improve the mobility of carriers.

Chapter 2

Poly-(3 hexylthiophene) (P3HT)

2.1 Introduction

Poly-(3 hexylthiophene) (P3HT) is a conjugated polymer commonly used as a photoexcitable absorber in polymer solar cells. This chapter focuses on the determination of the crystalline morphology of P3HT by *ab initio* methods: the crystallographic parameters of the lattice, as well as the coordinates of the atoms contained into the primitive cell have been optimized to find the packing with minimal energy. The optimized packing is used as input for the simulation of x-ray diffraction (XRD) powder diffraction pattern, which is compared with experimental data available in current literature. The electronic energy band structure of crystalline P3HT is then calculated and discussed. The absorption spectrum for visible photons is calculated and compared with experimental data. Technical details about the numerical methods used are available in appendix A.

2.1.1 (Poly-)thiophene

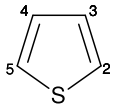

Thiophene (C_4H_4S) is a heterocyclic compound whose aromatic ring consists of four carbon atoms and one sulfur atom. Its chemical properties are similar to those of benzene (C_6H_6), in which the carbon orbitals are sp^2 hybridized in a ring structure made of σ bonds surmounted by three delocalized π orbitals. In thiophene, the sulfur atom ([Ne] $3s^2$ $3p^4$) contributes two electrons to the π orbitals so that the aromatic ring is completed with four carbon atoms.

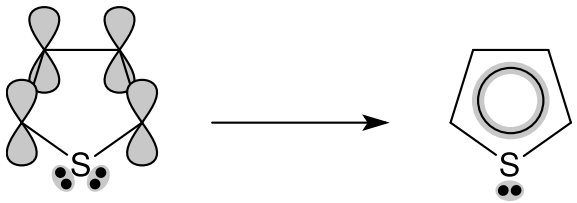

Figure 2.1. Thiophene aromaticity

Polymerization along the 2,5 carbon sites of thiophene leads to the poly-thiophene (PT) structure. The minimum energy ionic configuration for an isolated PT chain consists in a backbone made of thiophene rings disposed in alternating coplanar orientation. In poly-thiophene, adjacent aromatic rings constitute an effective conjugated system (see section 1.3.1) showing significant conductivity[1] upon appropriate doping. From k-space analysis it can be seen that the linear isolated PT chain system behaves as a direct gap semiconductor ($E_G \approx 2$ eV).

[1]Experimental conductivity measurements report figures ranging from 10^{-4} to 10^{-1} S/cm.

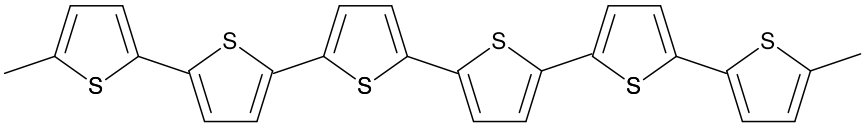

Figure 2.2. Poly-thiophene

Apart from high conductivity, poly-thiophene samples also show good thermal and environmental stability. Unfortunately, poly-thiophene is intractable, not being soluble in common industrial solvents. This lack of solubility is likely due to the strong π stacking interaction between the aromatic rings.

2.1.2 Side chain functionalization in poly-thiophene

The chemical structural graph for alkylthiophenes shows the addition of an alkyl side chain (R = C_nH_{2n+1}), which contributes to increased spacing between polymer backbones, so that π stacking is partially inhibited. As a result, the alkyl substituted polymer shows a significant improvement in its solubility. Poly-thiophenes with alkyl side chain substituted at site 3 are called poly-(3 alkylthiophene)s (P3ATs).

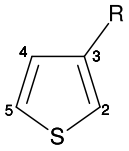

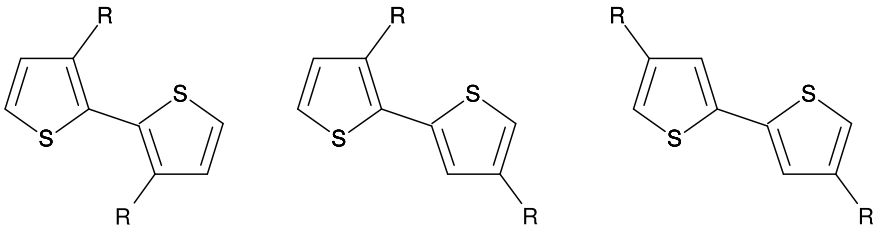

(a) head to head (b) head to tail (c) tail to tail

Figure 2.3. Possible regioisomers for alkylthiophene dimers

Another consequence of the addition of an alkyl side chain is the lowering of the spatial symmetry of the thiophene monomer. In particular, an alkyl substituted monomer is no longer symmetric with respect to reflection in the plane in which lie both the normal to the planar thiophene and the axis joining the sulfur atom with the center of mass, since site 3 is not equivalent to site 4. The three possible orientations for an alkylthiophene dimer are depicted in fig. 2.3. If the polymerization method is unable to select a particular sequential arrangement for the orientation of

the monomers, the polymeric chain is said to be *regiorandom*. In contrast, the establishment of a particular order in the sequence of the orientation of the monomers leads to a *regioregular* P3AT chain, the simplest of which is given by the repetition of head to tail (HT) dimers.

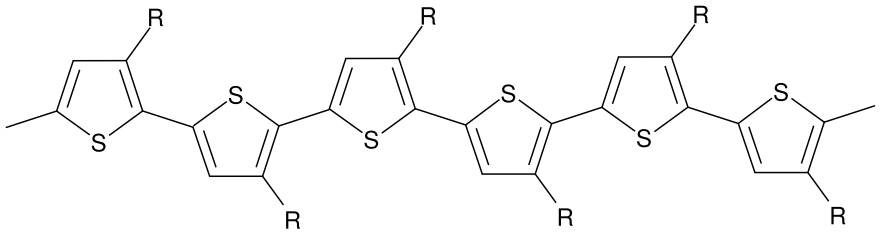

Figure 2.4. Regioregular HT P3AT polymer

2.1.3 Bulk properties

A number of physical properties have been found to be critically influenced by the degree of regioregularity of P3AT samples. It is understood that defects in the regioregular HT pattern induce twists between adjacent thiophene rings, resulting in reduced conjugation along the backbone and in general loss of supramolecular inter-backbone ordering. Conversely, the regular spacing between the alkyl chains is able to induce alignment between different backbones via van der Waals-like intermolecular forces. Traces of ordered packing mechanism of regioregular poly-alkylthiophene backbones have been observed in liquid phase [17] as well as in solid state [18, 19], where P3ATs usually assemble in lamellar domains. As expected, ordered packings show a lower optical band-gap than their disordered counterparts. In [20] this effect was observed in the redshift of the optical absorption onset, as well as in the enhancement of conductivity.

In several articles [21, 22] the dependence of film morphology and charge mobility on the molecular weight of poly-alkylthiophenes has been investigated. It was found that high molecular weight (MW) films typically show higher mobility than the low MW ones, which, however, appeared more crystalline in atomic force microscopy (AFM) images. The explanation for this apparently contradictory behavior is that charge transport properties of P3AT films are best described by a hopping model, in which longer polymer fibers can actually enhance the conductivity providing percolating "bridges" between semi-crystalline domains, as supported by experimental results found in [23] as well as in [24]. Molecular weight also seems to affect the crystalline packing: this point will be thoroughly discussed in subsection 2.2.2.

(a) Low Molecular Weight (b) High Molecular Weight

Figure 2.5. Bulk charge transport model in semicrystalline P3HT, adapted from [23].

The importance of understanding self-assembly mechanisms in poly-alkylthiophenes can not be underestimated, given its criticality in the control and reproducibility of optical and electronic properties of the active materials adopted in actual photovoltaic applications. Numerical methods have been mostly confined to the *a posteriori* reconstruction of possible unit cells from experimental diffractive data; a few published works deal with DFT based optimization of various P3HT structural models, which however are either limited to oligomers or constrained systems optimized with respect to a low number of geometrical degrees of freedom. Possible reasons that can limit the interest for *ab initio* quantum mechanics (QMs) calculations may involve the difficulties related to the inclusion of van der Waals interactions in the simulation of crystal packing. As fully detailed in appendix A, our approach takes advantage of a recently developed code which successfully incorporates London dispersion interactions by a semi-empirical approach [25], resulting in improved convergence to an energetically stable packing in molecular crystals.

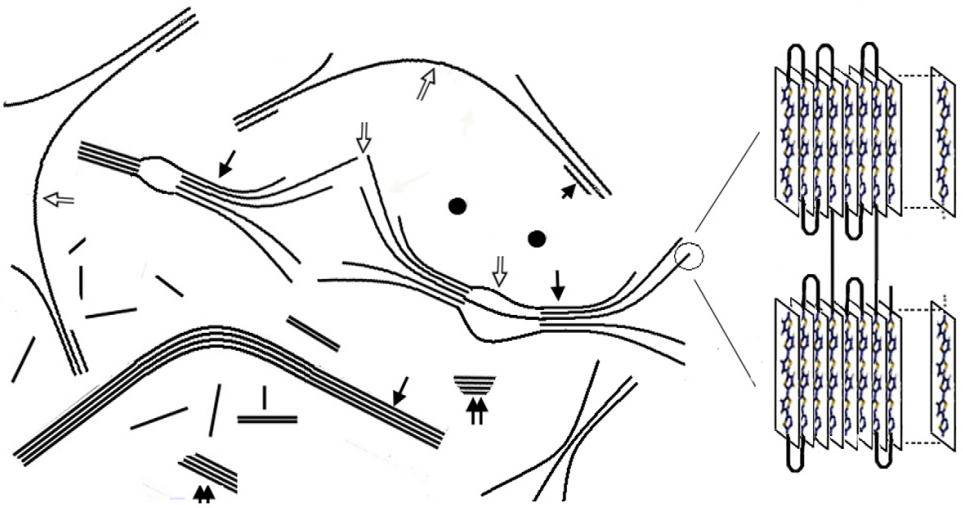

Figure 2.6. AFM observed lamellar packing in crystalline P3AT domains, reproduced from [26]. Black arrows mark zones of significant van der Waals packing between adjacent fibrillæ.

2.2 Theoretical modeling and numerical results

The focus of this chapter is the determination of the unit cell structure for crystalline domains of P3HT, which is the most commonly used P3AT for organic solar cells. Such a goal is reached with the stepwise optimization of increasingly complex structures, a path which is outlined in the present section.

The first step (subsection 2.2.1) involves the analysis of the isolated thiophene molecule; the introduction of monodimensional translational symmetry allows the treatment of one isolated polythiophene chain. The addition of the hexyl side chains to the PT polymer leads to the isolated P3HT polymer, whose optimized structure parameters are used as starting point for the optimization of the crystalline three-dimensional P3HT (subsection 2.2.2). Experimental data available in the literature are used to validate the numerical results. For the optimized cell structure XRD spectra are numerically evaluated and compared with actual experimental measurements. Finally (subsection 2.2.3), electronic and optical properties are derived and compared with their experimental counterparts. The analytic and numeric procedures adopted are presented in appendix A.

2.2.1 Preliminary analysis

Isolated thiophene molecule

The building block of P3ATs is represented by the thiophene ring. As detailed in the introduction, a thiophene molecule consists of a pentagonal ring made of four carbon and one sulfur atoms, with four additional hydrogen atoms each bound to a carbon site, thus totaling nine atoms per molecule. In this preliminary calculation, the electronic degrees of freedom (44 electrons) were represented within a minimal STO-nG basis.

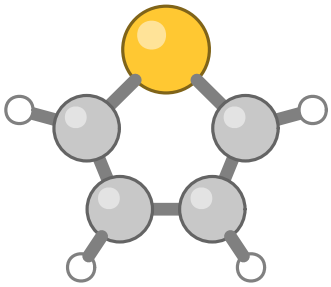

Figure 2.7. Optimized geometry for the isolated thiophene molecule.

The total energy of the system was minimized with respect to the ionic degrees of freedom without enforcing any space symmetry, leading to the structure reported in figure 2.7. Various symmetries in the placements of the atoms as well as the planarity of the system suggest that it belongs to the point group of the water molecule (Schönflies C_{2v}, Hermann-Mauguin mm2); a subsequent run enforcing this particular spatial symmetry confirmed the energetic equivalence between the two structural outputs.

A plot of the Kohn-Sham (KS) B3LYP Hamiltonian eigenvalues of the isolated thiophene molecule is reported in figure 2.8. A graphical representation of the squared modulus of the two highest occupied molecular orbital wavefunctions (MO 21 and 22) is reported in figure 2.9.

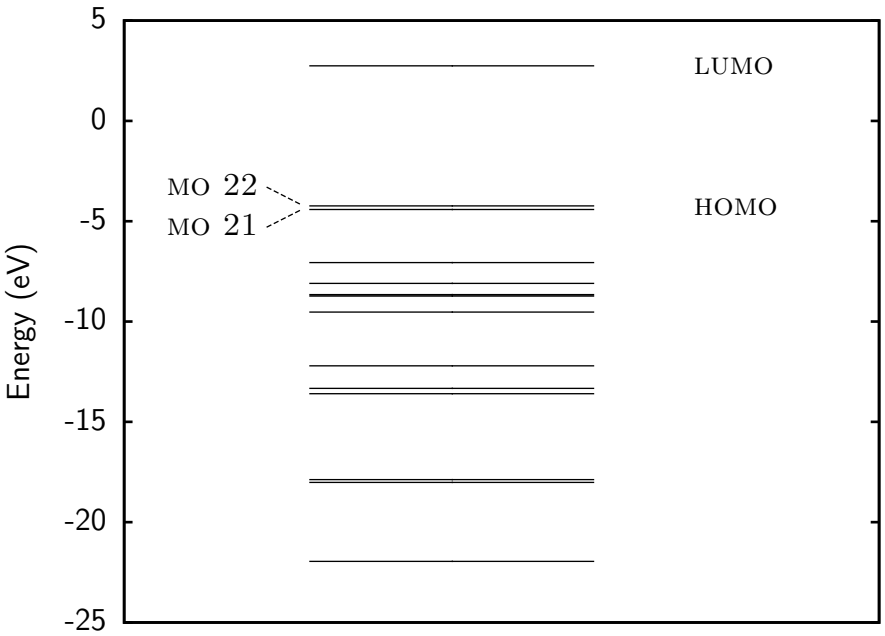

Figure 2.8. Highest occupied electronic energy eigenvalues for the isolated thiophene molecule. (B3LYP)

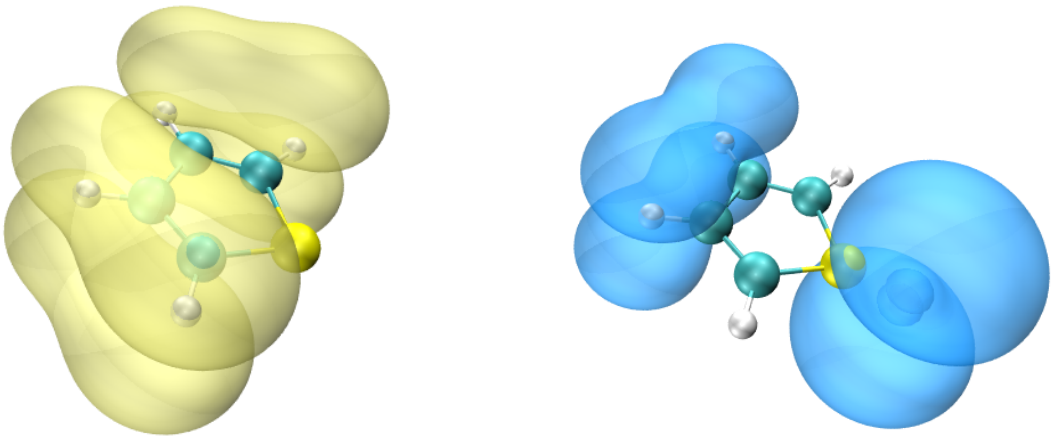

(a) MO 21 (b) MO 22

Figure 2.9. Squared modulus of the two highest occupied molecular orbitals in thiophene.

Isolated poly-thiophene chain

Thiophene polymerization occurs at carbon sites 2 and 5 (see scheme at pag. 21). The primitive cell of the crystalline polymer contains two monomers, each of which consisting of four carbon, one sulfur and two hydrogen atoms, thus totaling 14 atoms per cell. The electronic degrees of freedom (84 electrons) were represented within a minimal STO-nG basis. The minimization of the total energy of the system included both the translational lattice parameter and the full set of the internal ionic coordinates, without enforcing any other space symmetry. The resulting structural output (reported in figure 2.10(a)) is consistent with the rod group generated by a c/2 screw axis and the sulfur atom lying in a mirror plane orthogonal to ĉ (Schönflies C_{2h}^2, Hermann-Mauguin P 1 1 $2_1/m$); a subsequent run enforcing this additional space symmetry confirmed the correctness of this hypothesis. For the single chain polythiophene polymer structure the cell periodicity parameter is $c = 7.90$ Å. A graphical representation in direct space of the squared modulus of the valence band electron wavefunction is given in figure 2.10(b).

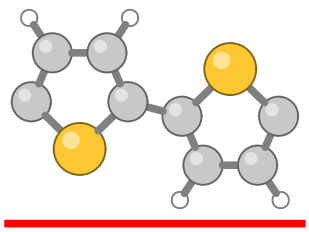

(a) Optimized geometry of the primitive cell

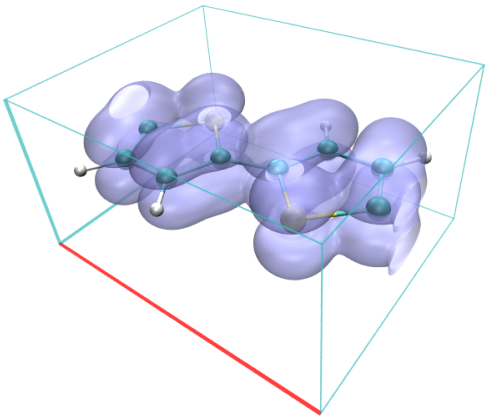

(b) Direct space localization of the valence band electrons

Figure 2.10. Graphical representation the isolated polythiophene polymeric chain. The lattice constant (red segment) is $c = 7.90$ Å.

Isolated poly(3-hexylthiophene) chain

The substitution of the hydrogen atom attached to carbon site 3 of the monomers in polythiophene with an all-trans hexyl tail (C_6H_{13}) provides a reasonable starting point for the optimization of the isolated HT-P3HT polymer chain, the hexyl tails being coplanar with the thiophene rings and orthogonal to the backbone of the polymer. As for the polythiophene, the unit cell contains two hexylthiophene monomers, thus totaling 50 atoms. As detailed in appendix A, the valence electronic degrees of freedom are represented within a gaussian basis, while core electronic states in carbon and sulfur atoms are embodied in Durand pseudopotentials. Both ionic and cell degrees of freedom have been optimized with the inclusion of van der Waals forces.

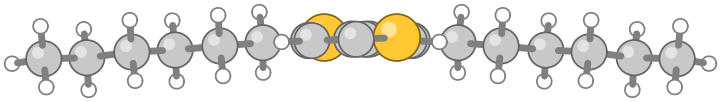

(a) *ab* plane

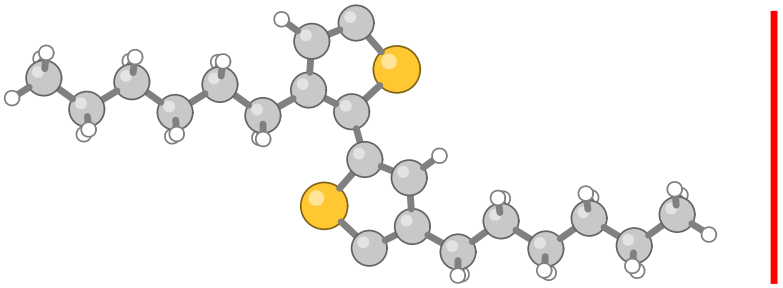

(b) *ac* plane

Figure 2.11. Optimized structure for the isolated P3HT polymer. The lattice constant is $c = 7.5$ Å.

The optimized structure (figure 2.11) shows that the thiophene backbone rings are coplanar, while each hexyl tail is in all-trans planar configuration, but slightly tilted towards the π stacking direction (positive $\hat{\mathrm{b}}$ axis). The periodicity along the conjugation direction is $c = 7.5$ Å, and the atoms in the unit cell can be contained in a box of 20.4 Å along $\hat{\mathrm{a}}$ and 2.1 Å along $\hat{\mathrm{b}}$. The computed energy band structure

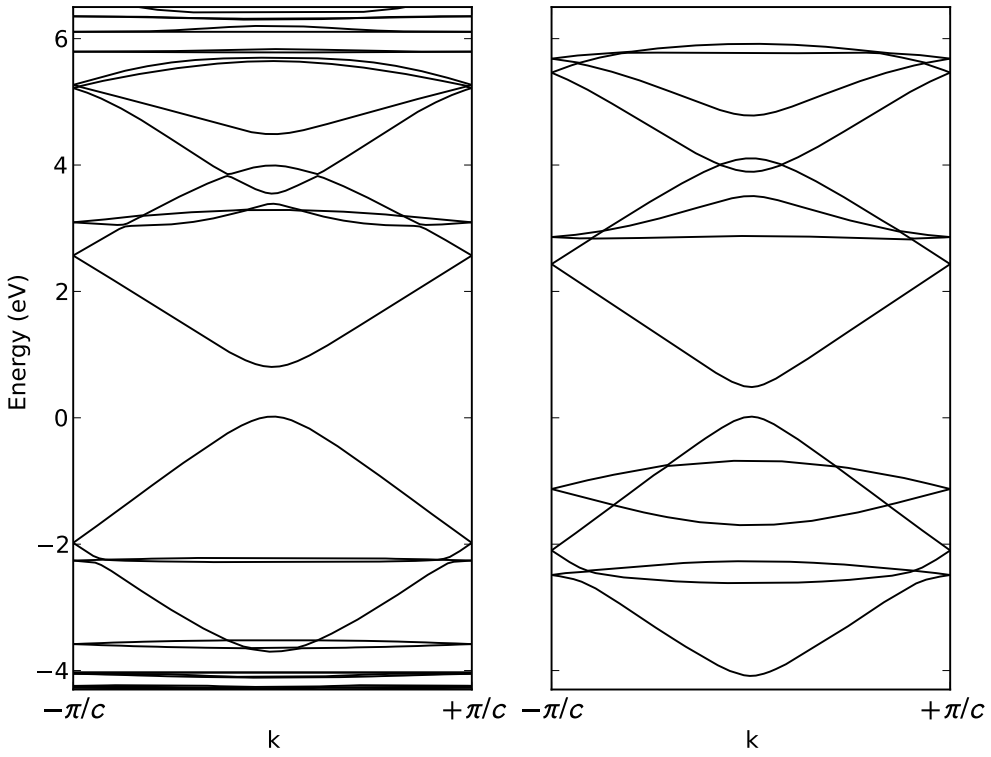

Figure 2.12. Band structure for the isolated P3HT polymer (left) and for the isolated polythiophene polymer (right).

is reported in figure 2.12, in which a direct comparison with the polythiophene calculation confirms that the near gap band features are mainly due to the thiophene electronic states, *i.e.*, the hexyl tail electronic states are not directly involved in the near gap band structure.

2.2.2 Three dimensional crystalline P3HT

Choice of crystalline unit cell

The determination of the crystallographic lattice class and parameters for crystalline P3HT is by no means trivial, being dependent on the packing model inferred by available x-ray diffraction (XRD) data. Usually, three directions are assigned to the packing of the P3HT chains:

- â: van der Waals hexyl side chain packing
- $\hat{b}$: thiophene π stacking
- ĉ: polymerization along the conjugation axis

While the first studies about the structure of crystalline domains of regioregular P3HT focused on high molecular weight samples, it was later found that the lowering of the molecular weight of P3HT polymers used in the preparation of thin films was correlated to a higher overall degree of crystallinity of the annealed samples. Low molecular weight P3HT films may show crystalline polymorphism, and the crystalline cell inferred from diffractive data deviates significantly from the case of high molecular weight films [23]. There are several indications that the crystalline unit cell for low molecular weight P3HT is monoclinic, while it is orthorhombic for high molecular weights. The cell parameters are summarized in table 2.1.

ref.	a (Å)	b (Å)	c (Å)	α (deg)	β (deg)	γ (deg)	M_w (kDa)
[27, 28]	15.9	7.5	7.6	90	101	90	2.5
[24, 29, 30]	16.0	7.8	7.8	90	90	93.5	5.7
[31]	15.73	7.66	7.66	90	90	93	5.2
[32]	33.6	7.66	7.70	90	90	90	80
[33]	16.63	7.75	7.77	90	90	90	–
this work	16.76	7.52	7.94	90.1	89.9	90.2	–

Table 2.1. Crystalline unit cells proposed for regioregular P3HT.

Since our *ab initio* structural optimization holds in the limit of an ideal crystal, the structural results must be compared with the high molecular weight diffractive data. The lattice class for high molecular weight regioregular P3HT is usually recognized as orthorhombic (see table 2.1). The two most broadly recognized periodicity features in (semi-)crystalline P3HT aggregates regard π stacking direction $\hat{b}$ and the

side alkyl direction â. Under wide angle XRD[2], the former usually appears as a rather broad halo centered at $2\theta \approx 24$ deg, while the latter is commonly associated with a distinct harmonic series at $2\theta \approx 5.2, 10.4, 16.4$ deg. These angular measurements are consistent with a choice of $a \approx 16.8$ Å and $b \approx 3.8$ Å, *or multiple thereof*[3]. The diffraction peaks related to periodicity along the direction of a primitive vector allow to determine a minimal value for that particular edge of the cell, but, in order to discriminate between possible choices for a supercell, one has to consider oblique[4] reflections. In the case of P3HT, the (111) reflection was independently measured in [32] for stretch-oriented films and in [33] for fibers. Both measurements are consistent with an orthorhombic cell containing two π stacked backbones ($b \approx 7.6$ Å), each composed of two head to tail (HT) alternated hexylthiophene monomers ($c \approx 8.0$ Å).

In the cell for the simulation of crystalline P3HT the two backbones are mutually shifted by c/2 along the conjugation axis in order to maximize the distance between the electronegative sulfur atoms, while the value for the â periodicity has been kept at $a \approx 16.8$ Å, since we could not find in current literature a compelling reason to consider a cell with $a \approx 33.6$ Å [5]. Overall, the input orthorhombic cell shows a volume of ≈ 1000 cubic Å, leading to an estimated density $\rho \approx 1.1$ g/cc, which is consistent with experimental measurements [32]. It is worth noticing that before the geometric optimization of the cell, the alkyl side chains, whose end-to-end length has been determined in subsection 2.2.1 to span 20 Å, experience significant interdigitation along the â direction.

Optimization of the crystalline P3HT structure

The input cell for the simulation contains four hexylthiophene monomers arranged in two π stacked backbones, thus totaling 100 atoms per cell. As with the isolated P3HT polymer, the valence electronic degrees of freedom are represented within a gaussian basis, while core electronic states in sulfur and carbon atoms are embodied in Durand pseudopotentials. Both ionic and cell degrees of freedom are optimized with the inclusion of van der Waals forces, and with the additional constraint of constant volume in order to exploit the experimentally known density to aid the convergence process. No spatial symmetry has been enforced, and triclinic deformations of the initial cell are possible.

[2] With x-rays from CuK_α source: $\lambda \approx 1.543$ Å.

[3] In fact, by doubling the modulus of a primitive vector of a Bravais lattice in direct space the corresponding reciprocal vector is halved, so that the former reciprocal lattice becomes a subset of the new one.

[4] *i.e.*, reflections having mixed Miller indexes.

[5] For the sake of completeness, we note that in [32] such a cell is proposed, but there are no well resolved oblique diffraction peaks whose indexing requires the doubling of the â edge.

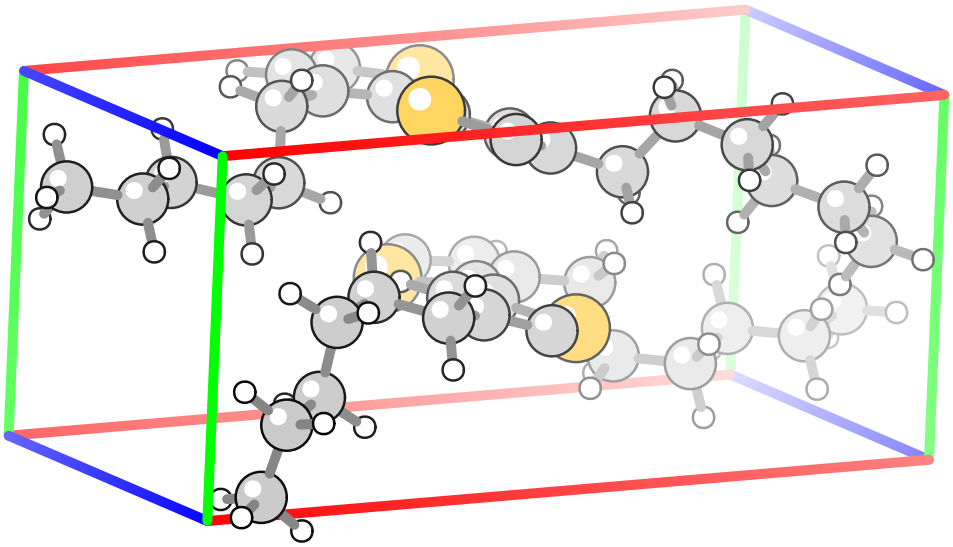

Figure 2.13. Optimized primitive cell for crystalline P3HT. White fog is added for depth cueing purposes. Red, green and blue segments indicate **a**, **b** and **c** vectors, respectively.

After convergence, the minimum energy structure (figure 2.13) shows an almost orthorhombic cell ($\alpha = 90.1$, $\beta = 89.9$, $\gamma = 90.2$ deg), with edge parameters $a = 16.76, b = 7.52, c = 7.94$ Å. It is also apparent that interactions between side chain induce structural changes in the geometry of adjacent thiophene rings, which are no more coplanar, but experience a slight torsion of about 16 degrees around the axis of the backbone. The arrangement of the side chains as viewed from the *ac* plane follows a fishbone pattern, while projection in the *ab* plane shows a complex packing structure in which each side chain fully exploits tridimensional space in order to minimize the packing energy (fig. 2.14). It is also worth noticing that the five terminal carbon atoms of each side chain are in all-trans staggered conformation, as in the isolated chain, but lie in a plane rotated around the attaching bond to minimize repulsive interactions with neighboring alkyl side chains. Overall, the side chains show no significant interdigitation.

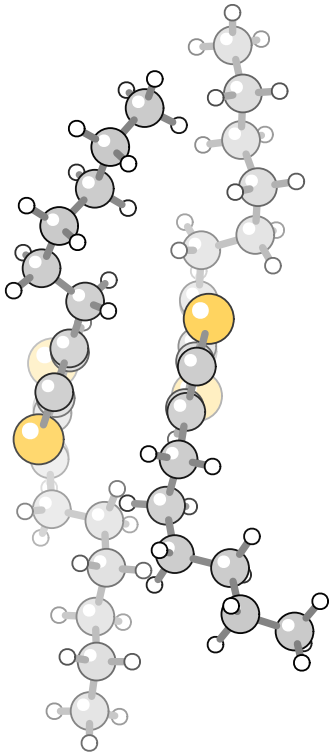

(a) Cell, (*ab* plane)

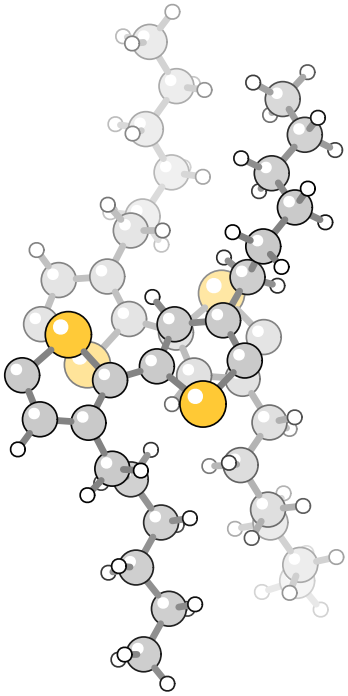

(b) Cell, (*ac* plane)

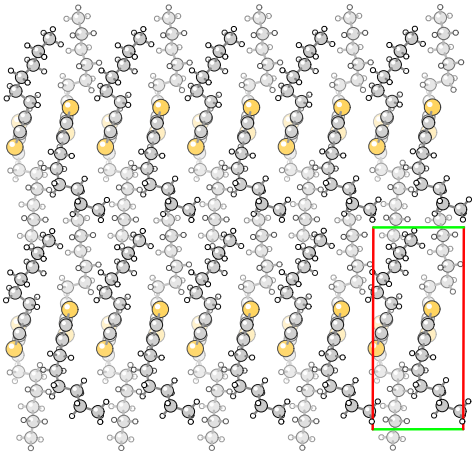

(c) Packing, (*ab* plane)

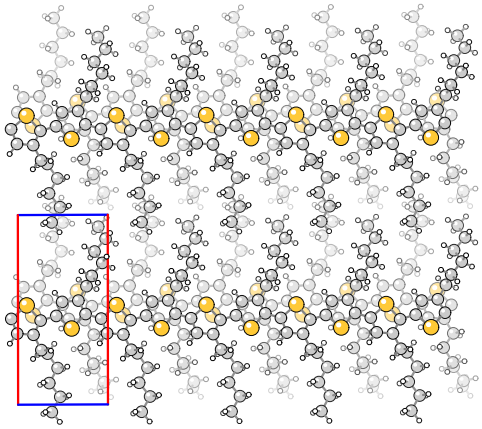

(d) Packing, (*ac* plane)

Figure 2.14. Optimized 3D crystalline P3HT morphology.

X-ray diffraction powder pattern simulation

The energy-optimized structure for crystalline P3HT has been used as input for the simulation of the XRD powder pattern, which has then been compared to the data[6] in [32] (figure 2.16). The goal for this comparison is not to guess a structure which fits the XRD experimental data (as in the Rietveld method), but to check if the results of the structural optimization are able to reproduce most of the diffractive features experimentally observed while concurrently allowing for small discrepancies in the position or intensity of the peaks, due to the effects of temperature, disorder and strain-induced dislocations in the samples.

The lattice reflections are classified according to the (hkl) Miller indexes. In particular, it is evident that the most important equatorial features at $2\theta \approx 5.2$, 10.4 and 16.4 deg, labeled as (h00), are well reproduced by the calculated profile. These features arise from first and successive reflections due to polymer chains being stacked along â by 16.8 Å. The other broad equatorial peak at $2\theta \approx 23.4$ deg, labeled as (h20) is consistent with an intralayer chain-to-chain spacing of 3.8 Å. Scattering intensities arising from the l = 1, 2, 3 reflections, reported in the insets of figure 2.16 to follow the style of the cited article, produce diffraction features which are similar to the experimental data.

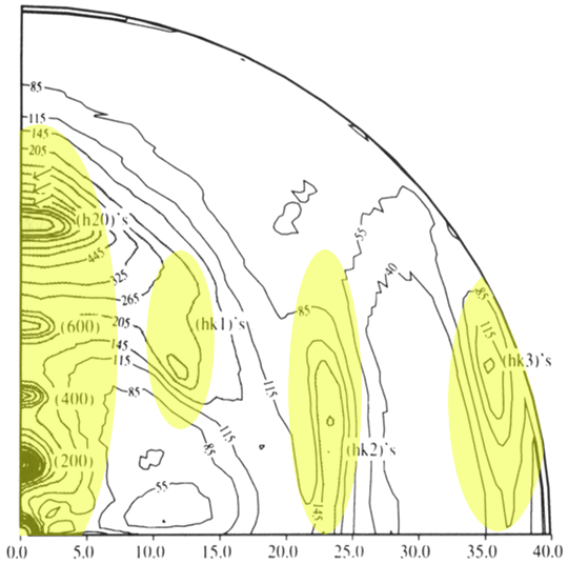

Figure 2.15. XRD data map published in [32]. In this graphical rendition, the reflection with different values for the l index are highlighted.

[6]Experimental XRD data have been numerically extracted from the digital bitmap image of the electronic version of the paper, corrected for background profile and XRD geometrical, Lorentz and polarization factors.

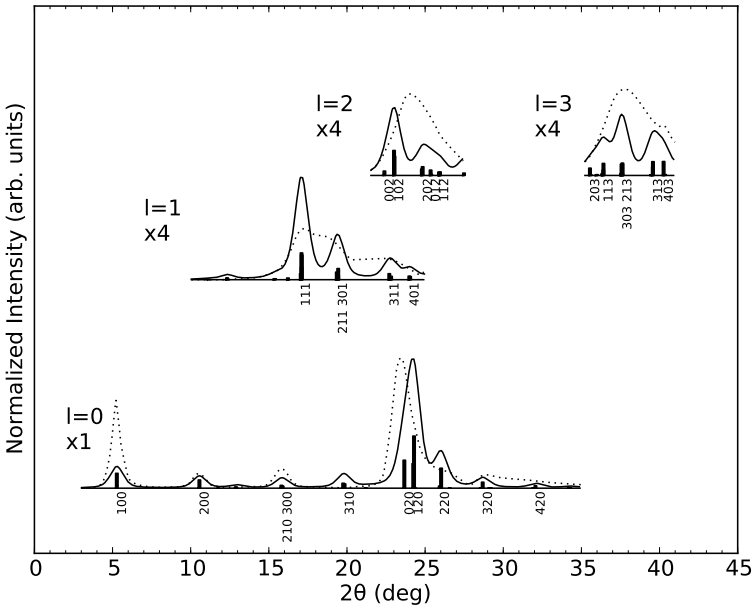

Figure 2.16. X-ray experimental [32] (dots) and calculated (lines) diffraction profiles for the optimized crystalline HT-P3HT polymer; vertical bars indicate lattice reflections. The experimental data was numerically extracted from the published electronic bitmaps of the graphs in [32], in which reflections arising from different values for the l index were independently resolved and measured. All diffraction profiles have been corrected for background halos, and XRD geometrical, Lorentz and polarization factors, so that the height of the peaks is actually proportional to the square of the structure factors (see also appendix A).

For the sake of completeness, we also consider the case of a crystalline cell containing a single polymer backbone ($b \approx 3.8$ Å, in this case). The resulting optimized structure is shown in figure 2.17(a). At a glance, considerable tilting between the two adjacent monomers can be appreciated; this distortion likely results from the strain induced by the close packing of translationally equivalent atoms along the π stacking direction. The XRD diffraction profile resulting from a supercell[7] built stacking two of this structures in the π direction is shown in figure 2.17(b) compared with experimental data [32].

[7]As required for consistent Miller labeling of peaks.

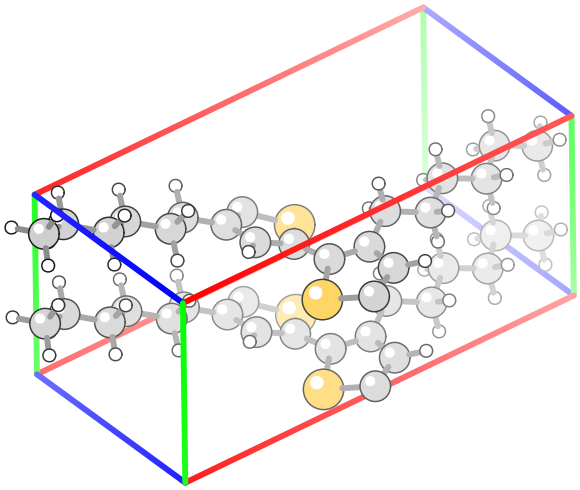

(a) Primitive cell

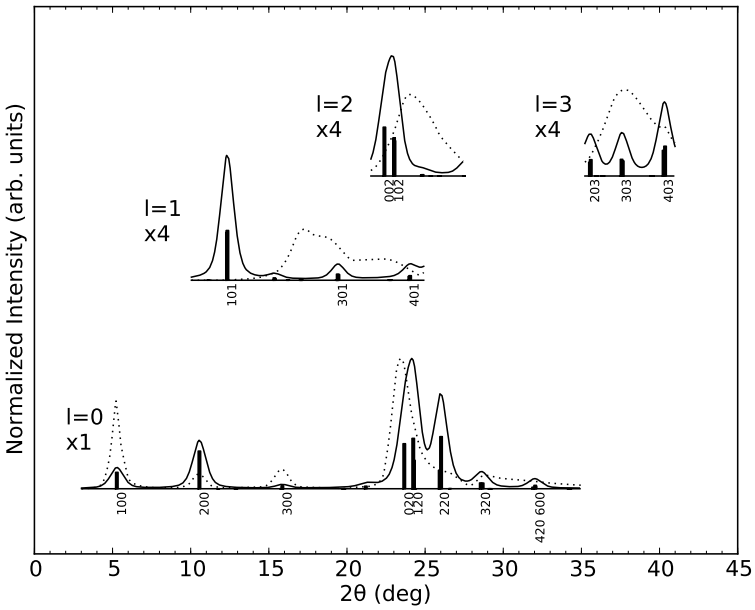

(b) XRD simulation: experimental [32] (dots) and calculated (lines) profiles

Figure 2.17. Structural and x-ray simulations for the optimized crystalline HT-P3HT polymer *having a single chain per cell.*

Due to the halving of the b parameter any reflection having an odd Miller k index is now suppressed, including the experimentally observed (111) oblique reflection. Also, an experimentally unobserved (101) reflection prominently emerges from the simulation of the $l = 1$ diffraction profile; this particular reflection is not present in the diffraction profile simulation reported in figure 2.16 for the case of two chains in the primitive cell due to destructive interference between the two translationally nonequivalent shifted backbones. We conclude that a primitive crystalline cell containing a single polymer backbone *cannot* satisfactorily reproduce experimental data.

2.2.3 Electronic and optical properties of P3HT

Energy Bands

Density functional theory (DFT) methods are known to systematically underestimate the energy band gap; this behavior is due to the fact that in KS-DFT ground-state energy is computed (exactly, in principle) on a convenience basis set (the KS orbitals) which does not formally correspond to a set of physical mono-electronic states. Even so, KS band structures result quite accurate in the depiction of valence and near gap conduction states, provided a semi-empirical correction of the gap width by means of a "scissor operator" is performed.

The energy band structure has been calculated for the optimized crystalline P3HT structure (figure 2.13), whose primitive cell is orthorhombic and contains two nonequivalent π stacked polymer backbones. The resulting band structure is presented in figure 2.18. The KS energy gap is 0.62 eV, a value that is lower (as expected) than the experimental optical absorption edge, which is about 1.9 eV as measured for this polymer, so that a scissor operator of 1.28 eV has been applied before calculating the optical properties. A certain similarity with fig. 2.12 can be noticed. In fact, it can be argued that the presence of two translationally nonequivalent polymer backbones causes a gemination of the single-backbone near gap states; this hypothesis has been confirmed by calculating the band structure in the single-backbone cell (fig. 2.17(a)).

Dielectric function and optical absorption

From the calculated electronic energy band structure the dielectric function and optical absorption have been calculated. The reference for the numerical methods used in this simulation is presented in appendix A.

The real part of the dielectric function averaged over transverse and parallel polarizations is shown in figure 2.19(a), plotted against experimental data from Logothetidis *et. al.* [34]; the simulation with a scissor operator of 1.28 eV and an

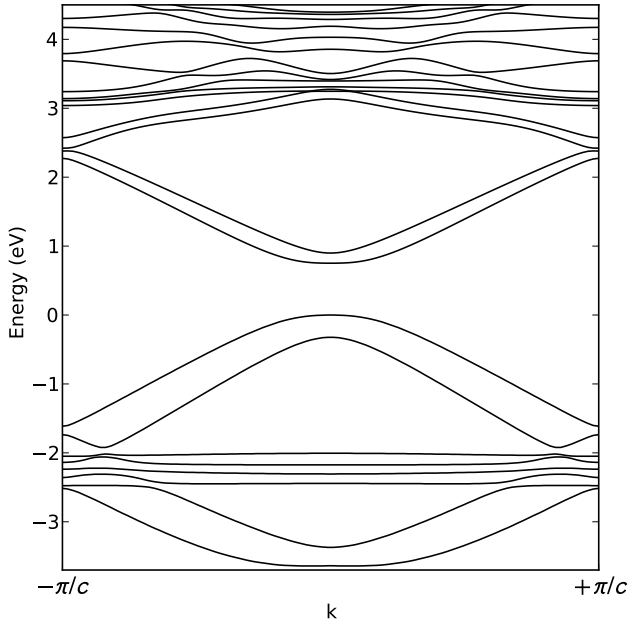

Figure 2.18. Near gap energy band structure along the conjugation axis of crystalline P3HT. The DFT gap is 0.62 eV wide.

energy smear of $\hbar\gamma = 0.2$ eV shows a strong agreement with the experimental data. The optical absorption has been derived from the imaginary part of the dielectric function:

$$\alpha(\omega) = \omega\frac{\epsilon_2}{nc}$$

A direct comparison (figure 2.19(b)) between the calculated absorbance and the actual measurements performed by Ohkita *et. al.* [35], shows overall agreement between the experimental data and the numerical calculation. In particular, a distinct series of absorption peaks can be identified. In our simulation, this series (marked by arrows in figure 2.19(b)) is due to the gemination of the conduction and valence bands (see figure 2.18). Experimental absorption data also present this feature as a set of three broad absorption peaks, who have been so far attributed to transitions of excitonic or vibronic character. The reproduction of these effects by the simple mono-electronic model proposed in this work is noteworthy.

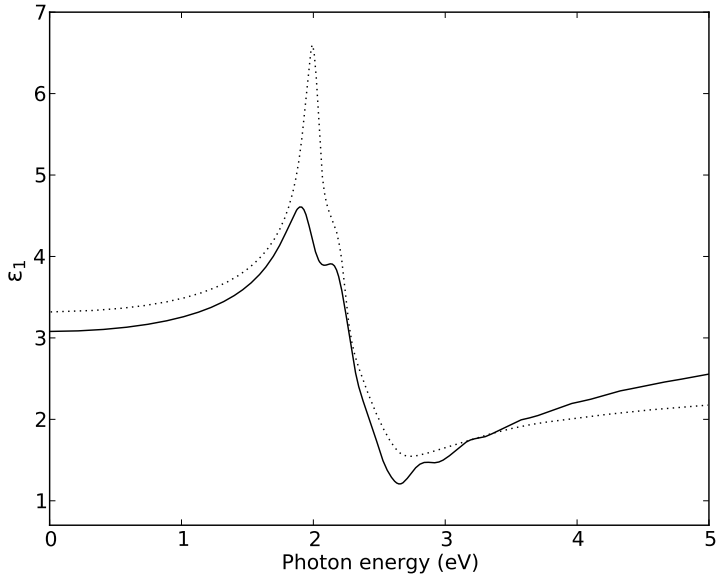

(a) Real dielectric function

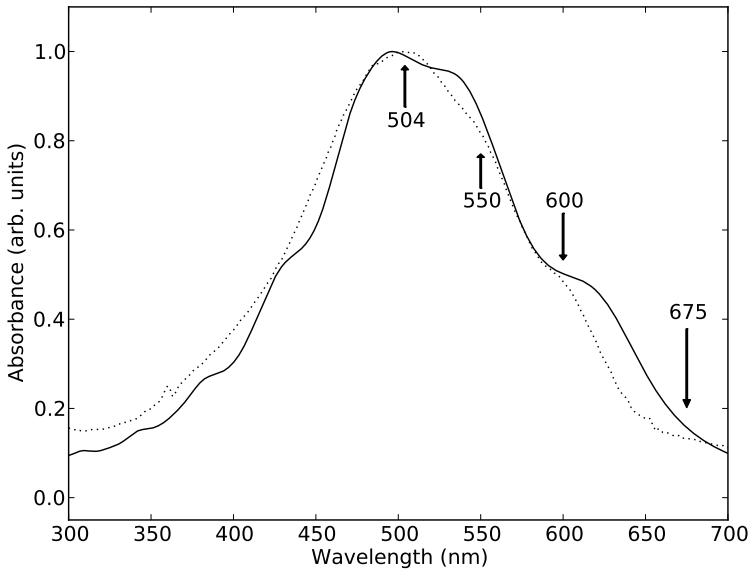

(b) Optical absorption

Figure 2.19. Optical properties of crystalline P3HT (continuous line: calculated values, points: experimental data).

2.3 Summary of the chapter

A model for the crystalline HT-P3HT has been proposed, in which the primitive cell is almost orthorhombic with the following parameters:

a (Å)	b (Å)	c (Å)	α (deg)	β (deg)	γ (deg)
16.76	7.52	7.94	90.1	89.9	90.2

The primitive cell contains four hexylthiophene monomers arranged in two π-stacked backbones, with a relative shift of c/2 along the conjugation direction. The hexyl tails appear not to be interdigitated between adjacent cells, exploiting the available space, being driven by van der Waals interactions to reach such a close packing. A central result of this work is the consistency with experimental XRD data. It has been shown that the "single backbone per cell" model cannot successfully reproduce the same experimental data.

The presence of two different polymer backbones in the primitive cell affects the energy band structure of the model. A distinct gemination of the conduction and valence band is observed; the resulting monoelectronic optical properties show an overall match with their experimental counterparts provided a scissor operator of 1.28 eV is applied to the band gap.

It is worthy of note that well resolved experimental absorption spectra for P3HT typically feature a series of three broad absorption peaks, which are indicated in figure 2.19(b) by arrows. This series has also been interpreted as originating from transitions between different vibronic states or being due to exciton-like phenomena; however, it is remarkable that the mono-electronic band structure calculated for crystalline P3HT is able to interpret these features in the absorption spectrum without additional *ad hoc* models.

In order to provide a robust optoelectronic model for light absorption in crystalline P3HT, collective electronic phenomena such as excitons as well as couplings with the ionic degrees of freedom should be taken into account. Such analysis exceeds the scope of the present thesis.

Chapter 3

Phenyl-C61-butyric acid methyl ester (PCBM)

3.1 Introduction

Phenyl-C_{61}-butyric acid methyl ester (PCBM) is a fullerene derivative[1] used as an electron acceptor in polymer solar cells. The role of the acceptor concerns the charge separation process of excitons obtained by photoexcitation in the donor domain. This process consists in a fast transition between the excited state of the donor conjugated polymer and an excited state of the fullerene molecule. The fast charge separation effect was experimentally observed in [37], and in a recent theoretical work the main features of this process were discussed [38]. The analysis of charge photogeneration in P3HT/PCBM blend films has been carried out in [35, 39].

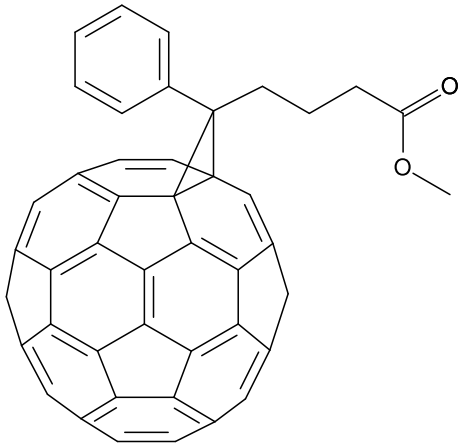

Figure 3.1. The chemical structure of PCBM

This chapter focuses on the determination of the not yet definitely assessed morphology of PCBM crystalline domains in PSCs. Packing models related to different crystallographic lattice symmetries are reviewed and compared to experimental data. The geometric optimization of each model, with methods described in appendix A, allows the establishment of a ranking table for the packings, whose indexing is dictated by minimum energy arguments.

3.1.1 PCBM in bulk heterojunctions

In polymer solar cells a (disordered) bulk heterojunction is typically obtained by casting a liquid solution of donor and acceptor constituents and subsequently annealing the resulting film. Different electrical and optical characteristics can be obtained, depending on processing parameters such as solvent used, annealing procedure and relative concentration between donor and acceptor constituents; these

[1] The addition of functionalized phenyl and ester groups improves the solubility, and hence the processability, of the C_{60} molecule [36].

parameters also directly influence the abundance as well as the morphology of the crystalline domains in the films. A comprehensive review can be found in [40]; here some major points are highlighted.

The precursor solution parameters involve type of solvent used, overall solution concentration and weight ratio between donor and acceptor solutes. In [41–43] the choice of the solvent appears to affect the size of the PCBM crystallites; aromatic solvents such as chlorobenzene (CB) yield small crystalline domains finely dispersed into the film, while samples cast from other solvents like toluene or chloroform typically show large scale phase separation between donor and acceptor domains, a feature which is also observed under high initial concentrations in the precursor solution. While small amounts of dispersed PCBM molecules are usually sufficient to split the excitons, as it has been verified by observing the quenching of the photoluminescence in the donor, a 1:1 weight ratio between PCBM and donor is typically required to achieve the highest efficiency for polymer solar cells (PSCs) due to the formation of percolating acceptor highways towards the relevant electrode [41, 44–46].

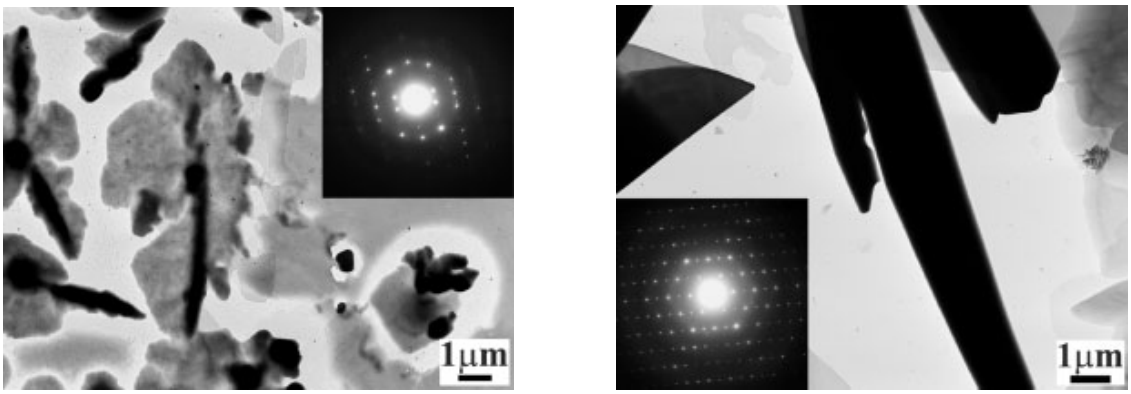

(a) Solvent: chlorobenzene (b) Solvent: toluene

Figure 3.2. TEM bright field and SAED patterns of PCBM crystals obtained by slow evaporation in solvent saturated atmosphere. Reproduced from [42]. Dark areas indicate PCBM crystals. Note the high symmetry in the SAED pattern of crystals obtained from toluene.

The casting method and post-casting treatment also influence the morphological and electro-optical features of the resulting thin films. During the casting, slow solvent evaporation rate allows the crystallization of micron-sized PCBM crystallites, whereas a fast solvent evaporation rate (as in spin casting) typically yields smaller nanocrystals finely distributed in the host polymer [42]. Thermal annealing results in improved diffusion of PCBM nanodomains in the donor matrix, as well as enhancement of the crystallinity of the donor itself; growth of visible PCBM crystallites is

also observed [47, 48]. Various other processing peculiarities, such as host polymer regioregularity degree [49] or use of surfactants [50] were also found to influence the size and distribution of PCBM domains.

3.1.2 Crystalline properties

Information about the crystalline unit cell of PCBM are seldom encountered in current literature. In [43] a sixfold axis was observed in selected area electron diffraction (SAED) analysis of PCBM crystallites, from which a face centered cubic (FCC) lattice was proposed under the assumption that the crystallization process was mainly due to the packing of the C_{60} part of the molecule[2]. However, the lattice parameter for this packing was estimated in 14 Å, yielding a cell volume of ≈ 700 cubic Å, which corresponds to a mass density of ≈ 2.2 g/cc, while the experimentally measured density is 1.5 g/cc [51].

In [52] an accurate XRD analysis is performed on platelet crystalline samples of PCBM obtained from two different aromatic solvents: chlorobenzene (CB) and orthodichlorobenzene (ODCB); the proposed crystalline cells contain molecules from both the solute as well from the solvent and are triclinic and monoclinic, respectively. As will be illustrated in subsection 3.2.4, the PCBM-ODCB cell is actually stable under *ab initio* geometry optimization, and the simulation of its XRD powder spectrum matches the data published in an independent experimental source [53]. The experimentally observed dependence of the electronic and optical properties from the different solvents is then possibly explained by the change in crystalline morphology, given that CBs become part of the PCBM crystal. The low symmetry of the PCBM-CB packing was also observed in [54], where a "distorted asymmetric body centered cubic (BCC) cell" has been proposed.

Some studies have been devoted to the epitaxial growth of PCBM on various substrates, aiming to achieve a controlled nanostructured growth of crystallites; owing to the lack of comprehensive XRD studies concerning the packing of crystalline samples of pristine[3] PCBM, some useful hints in the reconstruction of a sensible unit cell may be deduced from the geometry of the epitaxial substrate planes. In [55] a site selective nucleation of PCBM on Au(111) planes was observed. The PCBM molecules appear to form dimers which subsequently nucleate on the FCC surfaces of gold in one-layered herringbone patterns. As the PCBM deposits, more layers accumulate, and the regular pattern eventually evolves into amorphous aggregates. The dimer-to-dimer side distance was estimated to be ≈ 10 Å, consistently with the packing between two C_{60} molecules, while the length of a single dimer was estimated to be ≈ 21 Å. In [56] PCBM crystals were grown on the hexagonal (001) plane of mica. An

[2] The C_{60} crystal, fullerite, packs as a FCC lattice.

[3] *i.e.*, whose packing does not include solvent molecules.

incomplete unit cell of a=15.5 Å, b=10.0 Å, γ=90.0 degrees was proposed for PCBM crystals. In a recent work [57] micron sized hexagonal PCBM crystals were grown on various substrates by slow dip coating in solvent (chloroform) saturated atmosphere. The crystals exhibited $\approx$ 25 Å high terraces along the normal of the substrate, while transmission electron microscopy (TEM) analysis indicates interplanar distances of 4.9, 8.4 and 4.2 Å, consistent with a triangular lattice having periodicity of 9.8 Å.

Review of available XRD data

It is apparent that different manufacturing routes lead to distinct PCBM crystalline morphologies. The inclusion of aromatic solvents such as chlorobenzenes results in low symmetry lattices: the use of CB leads to a triclinic (space group P $\overline{1}$) lattice, while ODCB leads to a monoclinic lattice (P 2_1/n). Other solvents are not quite as popular, since it is generally observed that the solubility of PCBM is highest in chlorobenzenes, which are both aromatic and strongly polar molecules; chloroform shows fair solvating properties, and is used as an alternative to chlorobenzenes. Insofar, there have not been any experimental observations which could suggest the inclusion of chloroform molecules into a crystalline PCBM phase.

A number of journal articles report graphically the powder XRD profiles of samples cast from CB [47, 54, 58]. In the case of ODCB a single published XRD pattern has been found [53]. These XRD powder profiles have been extracted from the image bitmaps of the electronic version of the published articles and are here reproduced for convenience (fig. 3.3). XRD profiles observed from PCBM samples grown from chloroform are not so common in literature; yet they are of interest because it is believed that they represent samples of "pristine" PCBM, *i.e.*, where the crystalline phases are not subject to solvent inclusion. In figure 3.4 are reproduced XRD profiles from different crystalline samples: terraced hexagonal crystals grown from chloroform [57], annealed PCBM powder milled from chloroform cast film [59], and in plane and out of plane XRD scans of PCBM films grown from an unspecified solvent, possibly chloroform [45]. All of these data are badly conditioned, being affected by unfavorable signal to noise ratio, broad peaks or low resolution, so that a direct determination of the crystallographic parameters of the unit cell of "pristine" PCBM it is not possible.

In the following, symmetry related arguments will be used to attempt the construction of possible crystalline packing models for "pristine" PCBM; in particular the modeling will be oriented to the search of models compatible with the observation of six-fold axes (see inset in fig. 3.2(b)).

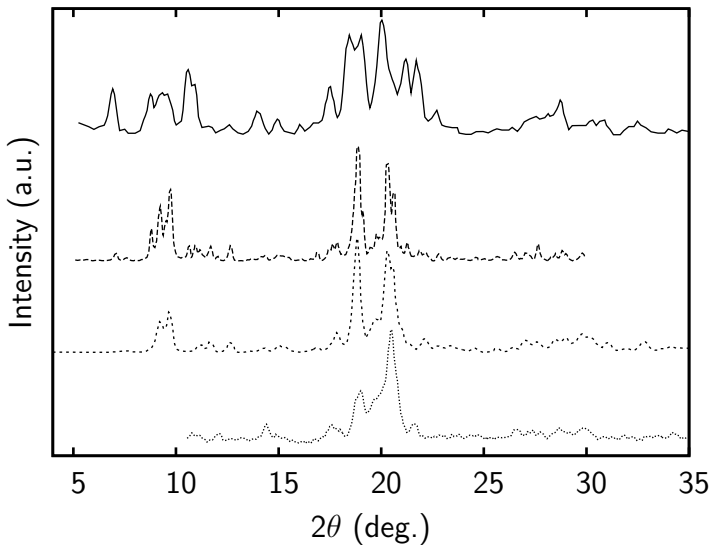

Figure 3.3. Powder XRD profiles from PCBM samples grown from ODCB (solid line) and CB (discontinuous lines) solutions. The different profiles have been shifted for clarity. From top to bottom, data sources are [53], [58], [47] and [54].

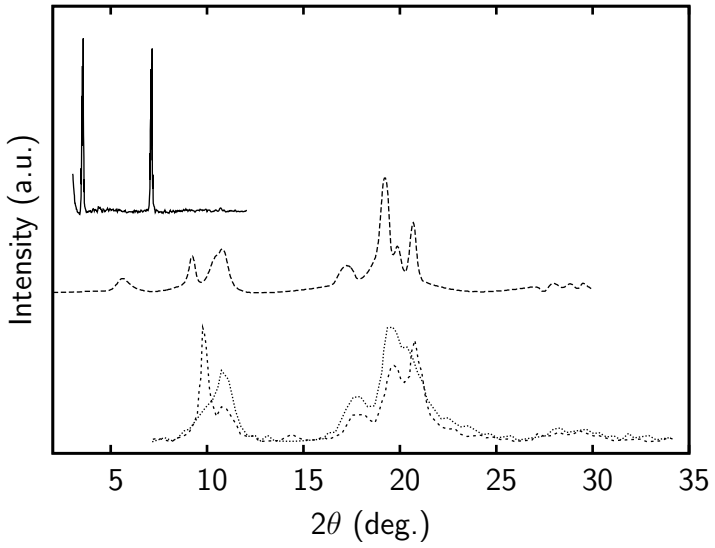

Figure 3.4. XRD profiles from PCBM samples grown from non-chlorobenzene solvents. The different profiles have been shifted for clarity. From top to bottom, data sources are [57] (terraced hexagonal crystals grown from chloroform), [59] (annealed powder grown from chloroform) and [45] (in plane and out of plane XRD scan of PCBM films grown from unspecified solvent).

3.2 Theoretical modeling and numerical results

3.2.1 Preliminary remarks

In this section symmetry arguments play a central part in the determination of the crystalline structure of PCBM. As an introduction to the actual investigation on the crystalline morphology of PCBM some brief remarks about crystallographic space group classifications are outlined below.

Crystal symmetry

The space symmetry group of an object consists in the set of spatial symmetry operations under which the object itself is invariant. In the case of a crystal, this comprises the translational subgroup as well as additional symmetry operations including reflections, rotations, rotoinversions, screw axes and glide planes. The translational subgroup is an abelian group of rank 3, whose elements can be isomorphously mapped into the Bravais lattice of the crystal. The Bravais lattices in three dimensions are grouped into 14 types, organized into 7 crystallographic lattice systems; two Bravais lattices are said to be equivalent if their space groups are isomorphic. The quotient of the space group by the Bravais lattice is called point group, since its elements are symmetry operations which leave one point fixed. The crystallographic restriction theorem limits the number of nonequivalent point groups to 32 crystallographic point groups. The complete space group of a crystal is then built by combinations of symmetries from the Bravais lattice and from the point group. There are 230 crystallographic space group types; they are enumerated and thoroughly examined in the International Tables for Crystallography [60].

An "empty" Bravais lattice has the highest space symmetry, every additional atom in the unit cell results in equal or lower point group symmetry for the cell and thus for the whole crystal: the space group of an actual crystal contains fewer or at most the same number of symmetry elements than the space group of its Bravais lattice. Moreover, a crystal with a given point group symmetry is classified as belonging to the crystallographic system having the *minimal* space symmetry needed to include all the elements of the point group [61]. This is because, even though the contents of a generic unit cell could in principle be arranged in a crystal lattice system with higher space symmetry than the cell itself, such an arrangement would be unstable against mechanical perturbations acting on the crystal. As an example, the unit cell used to model crystalline P3HT in the previous chapter has no point group symmetry elements beside the identical transformation; as such, the whole crystal belongs to the P 1 space group, which is triclinic. It was found that the energy-optimized cell was indeed triclinic, although very close to an orthorhombic cell.

Crystalline PCBM

In the tentative reconstruction of the crystalline morphology of PCBM, due to the partial lack of experimental data about the expected crystallographic lattice class, one has to resort to a heuristic exploration on various lattices, starting from appropriately constrained unit cells. This exploration is carried out following both a "bottom-up" as well as a "top-down" approach, in the sense of symmetry.

The "top-down" approach consists in testing high symmetry lattices belonging to the cubic and hexagonal classes, driven by the observation of a sixfold axis in [43], a symmetry feature which is only found in high-symmetry point groups. A triclinic cell with appropriate fixed parameters, corresponding to the primitive cell of an high symmetry lattice, was used as the input unit cell. Just as in the aforementioned case of crystalline P3HT, the optimized P 1 triclinic cell could end up being a slight distortion of a cell with higher symmetry. The drawback of this approach is that no point group symmetry can be exploited, and the largest unit cells that can be used for the modeling must contain a maximum of two PCBM molecules, the limiting factor being the available computational resources. This analysis is the subject of subsection 3.2.2.

The "bottom-up" approach consists in building unit cells belonging to proper space groups with increasing symmetry, considering symmetric unit cells containing up to four PCBM molecules. The symmetric unit cell is generated applying the appropriate symmetry operations of a given point group to the *asymmetric* cell, which consists in one PCBM molecule. This analysis is the subject of subsection 3.2.3.

Finally, the system PCBM-ODCB has been considered. In [52] the complete unit cell of this system has been determined by computer-aided diffractive analysis. The authors published online the full crystallographic data in a CIF file available in the supporting information section on the publisher website. These data were used as input for a full geometrical optimization. After the optimization a powder XRD pattern was calculated and successfully matched against experimental data from an independent source [53].

3.2.2 High symmetry constrained lattices

Cubic lattices

Initially, the cubic lattice class was explored. The cubic lattice class has the highest symmetry among the Bravais lattices, and the associated space groups contain threefold axes. Given that crystalline C_{60} packs as a FCC lattice at room temperature, the cubic class represents a possible candidate for the high symmetry packing of PCBM. A cubic Bravais lattice has one degree of freedom, which can be determined from the experimental mass density for PCBM films [51]: 1.5 g/cc. This corresponds to a volume of ≈ 1000 cubic Å per molecule of PCBM in the unit cell. This volume

corresponds to a rather close packing for all the cubic lattices; the PCBM molecule input model was manually oriented so that the functional group attached to C_{60} did not overlap with the nearest neighbors. The optimization was carried out by minimization of the electronic DFT-KS energy functional (E_{opt}: see A.14) in respect to the in-cell coordinates of the 88 atoms in the PCBM molecule and to the parameters of the primitive cell under symmetry constraint. In the case of cubic lattice class the only degree of freedom is the length of the edge of the cell. After the geometry optimization, each cubic lattice slightly varied its volume. The results are summarized in table 3.1, while a graphical representation of the cubic packings is presented in figures 3.5(a-c).

	a,b,c (Å)	α, β, γ (deg)	E_{opt} (at.u.)	ρ (g/cc)
SCU	10.15	90.0	-444.22836	1.445
BCC	11.10	109.5	-444.21425	1.432
FCC	11.60	60.0	-444.17869	1.369

Table 3.1. Results of the optimization of the cubic lattice structures containing one molecule of PCBM per unit cell. The simple cubic arrangement has the lowest energy and the highest density.

The simple cubic case shows the lowest energy per cell, a predicted mass density of 1.445 g/cc, which is rather close to the experimental value, with the nearest neighbors at 10.15 Å. The body centered cubic comes next, with mass density of 1.432 g/cc and nearest neighbors at 11.11 Å. Finally, the face centered cubic exhibits the highest energy per cell and the less dense packing, at 1.369 g/cc with the nearest neighbors at 11.60 Å. It is apparent that the simple cubic symmetry is the one which permits the functionalizing group to pack more efficiently, energy-wise and space-wise.

Hexagonal lattices

Another high symmetry lattice class which contains three-fold axes is the hexagonal lattice class. The hexagonal unit cell has two degrees of freedom: parameters a and c. The parameter a was set at 9.67 Å, while $c = 12.45$ Å was derived from the volume constraint. During the optimization c was varied, and the lowest energy was found for $c = 12.50$ Å, leading to a mass density very close to the experimental datum. The resulting energy is higher than the simple cubic but lower than the body centered cubic lattice. The hexagonal *monomer* packing is depicted in figure 3.5(d).

Due to the consideration that a significant electric field may be present in the neighborhood of the oxygen atoms composing the ester groups, a hexagonal cell featuring two independent PCBM molecules (a *dimer*) was devised. The input cell is

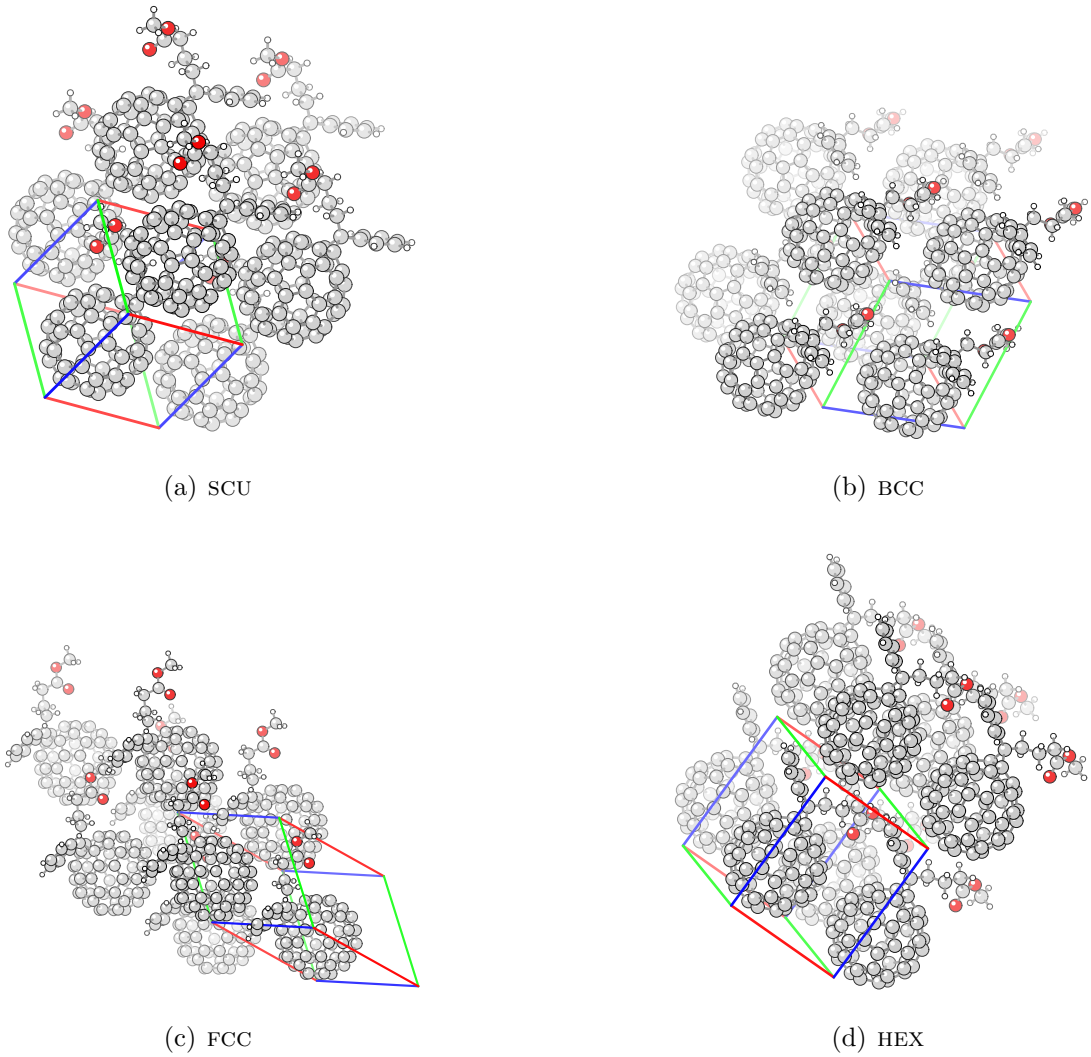

(a) SCU (b) BCC

(c) FCC (d) HEX

Figure 3.5. Graphical representation of optimized high symmetry cubic and hexagonal packings having one PCBM molecule per unit cell.

obtained by doubling the c parameter of the previous hexagonal cell. The functionalizing groups in the two PCBM molecules face each other, giving rise to intermolecular bonds which lower the energy (≈ -8 kcal/mol) in respect to the hexagonal packing with one PCBM molecule per unit cell. In fact, this arrangement (figure 3.6) results in the lowest total energy per monomer among all the high symmetry lattices. After the optimization the mass density actually increases to 1.536 g/cc, confirming the high efficiency of this packing. The hexagonal packings are reviewed in table 3.2.

N_{PCBM}	a,b (Å)	c (Å)	α, β (deg.)	γ (deg.)	E_{opt}/N_{PCBM} (at.u.)	ρ (g/cc)
1	9.671	12.50	90.0	120.0	-444.21945	1.493
2	9.671	24.30	90.0	120.0	-444.23223	1.536

Table 3.2. Results of the optimization of hexagonal lattices of PCBM. N_{PCBM} represents the number of PCBM molecules in the primitive cell. The *dimer* arrangement has the lowest energy and the highest density among the high symmetry constrained lattices which have been tested for crystalline PCBM.

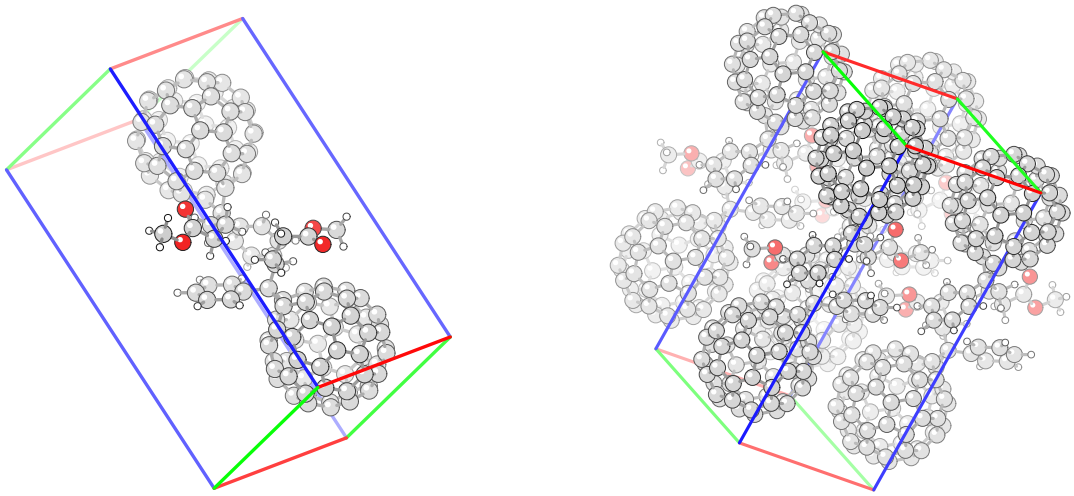

(a) Hexagonal unit cell

(b) Packing of hexagonal cells

Figure 3.6. Graphical representation of the optimized hexagonal lattice with two PCBM molecules per cell (*dimer*).

3.2.3 Low symmetry lattices: from hexagonal to monoclinic

Driven by the favorable packing energy obtained by the hexagonal dimer arrangement presented in the previous subsection, a proper "quasi-hexagonal" monoclinic space group has been considered. The general idea (fig. 3.7(a)) is to reproduce the triangular sublattice of the hexagonal packing with a centered rectangular face of height $a \approx 9.6$ Å, and width $b = \sqrt{3}a \approx 16.6$ Å. The input c parameter was set at 25.0 Å, with a monoclinic β angle of 94 degrees, which results in optimal alignment between the facing C_{60} layers. The first symmetry element of the symmetric unit cell is thus a translation of $(\mathbf{a} + \mathbf{b})/2$. The second symmetry operation addresses the construction of a facing dimer from a PCBM molecule. The easiest way

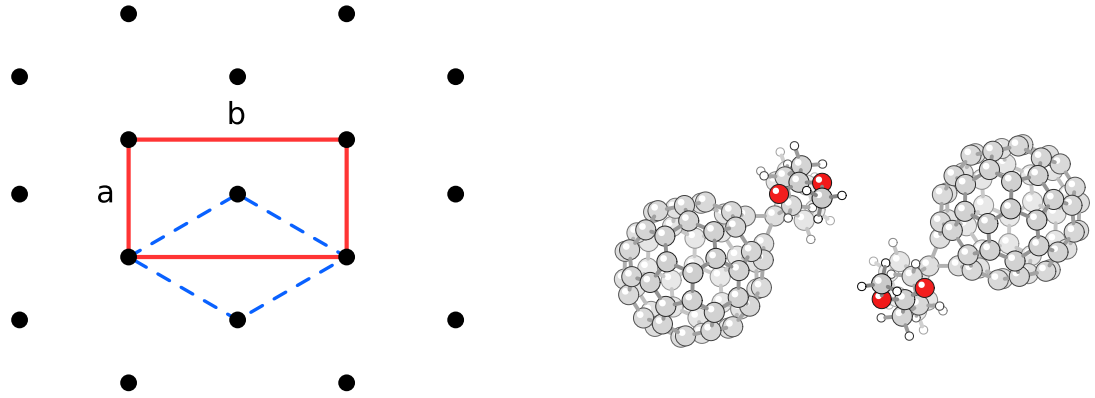

(a) Approximating the triangular lattice

(b) Construction of the PCBM dimer

Figure 3.7. Construction of the monoclinic cell C 2 as an approximation to the hexagonal *dimer* packing.

is to consider a rotation of 180 degrees around the b-axis. In figure 3.7(b) this particular symmetry element can be appreciated. The resulting space group has been identified as the monoclinic C 2.

	a (Å)	b (Å)	c (Å)	β (deg.)	E_{opt}/N_{PCBM} (at.u.)	ρ (g/cc)
fixed cell	9.60	16.65	25.1	93.99	-444.22488	1.51

Table 3.3. Results of the optimization the C 2 monoclinic lattice.

The input cell has been optimized with respect to the internal degrees of freedom, leading to the packing shown in figure 3.8, and whose parameter are reported in table 3.3. The resulting energy is close to that of the hexagonal dimer packing. Both the refined hexagonal and C 2 packings have been used as input cells for the calculation of the powder XRD profiles. A comparison between the calculated XRD profiles and the experimental data is shown in figure 3.9. It is evident that the C 2 cell correctly reproduces the (001) and (002) reflections, related to the 25 Å periodicity along the c edge. The hexagonal dimer cell features a strong reflection at $2\theta = 10.5$, related to an interplanar distance of 8.3 Å. In the case of the monoclinic C 2 packing, this particular reflection is almost quenched by symmetry, leading to a better match with the experimental data. It must be noted that the experimental data published in [57] is incomplete and badly conditioned. A more thorough experimental XRD analysis is required to confirm the monoclinic model proposed in the present work.

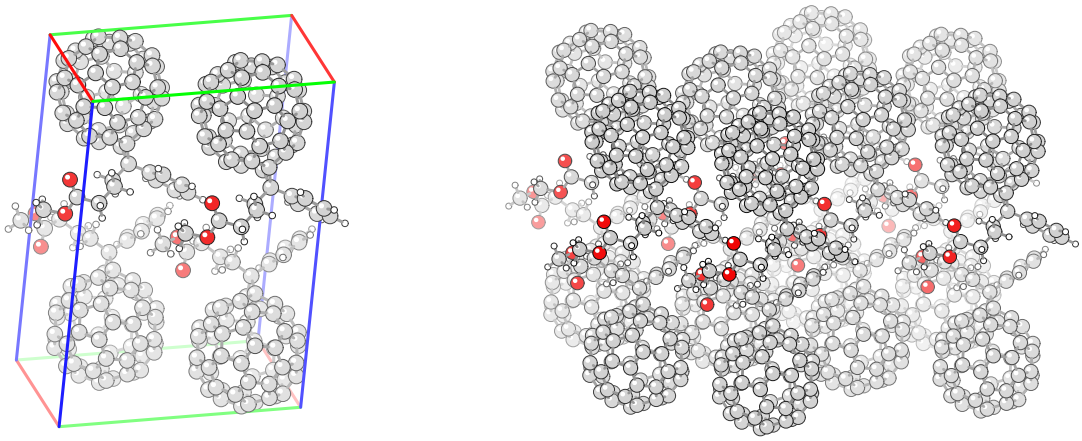

(a) Symmetric unit cell (b) Packing

Figure 3.8. Graphical representation of the monoclinic C 2 lattice

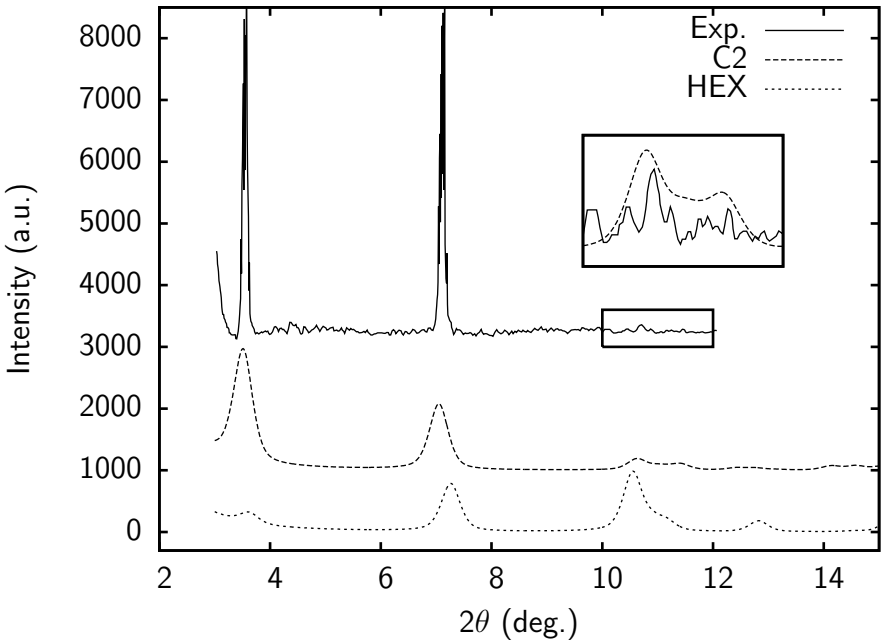

Figure 3.9. XRD calculated profiles (dashed lines) for the hexagonal dimer and the monoclinic C 2 packing compared with the experimental data from [57]. The curves have been shifted for clarity, while the inset shows a magnified view of the 8.3 Å region marked in the main plot. The intensities of the diffraction peaks in the experimental data are better reproduced by the monoclinic packing.

3.2.4 Monoclinic lattice with ODCB inclusion

As previously outlined, it has been observed that PCBM crystallized from chlorobenzenes results in different crystalline morphologies than PCBM grown from other non-aromatic solvents. In [52] a thorough crystallographic investigation was performed; the unit cell of crystals grown from CB and ODCB was determined by numerical methods on x-ray diffraction data. In either case it was found that molecules from the solvent were included in the unit cell. The PCBM-CB cell has been determined as triclinic, while the PCBM-ODCB cell as monoclinic.

This subsection aims to determine whether the proposed unit cell for the PCBM-ODCB is energetically stable. The atomic positions were extracted from the supporting information page on the website of the publisher. The asymmetric unit cell contains one molecule of PCBM and one molecule of ODCB, while the symmetric unit cell contains four PCBM and four ODCB molecules via the action of the symmetry operations in space group P 2_1/n. The symmetric unit cell is displayed in figure 3.10.

A full geometric optimization (over the coordinates of the 100 atoms in the asymmetric unit cell and four monoclinic parameters) has been performed under the constraint of P 2_1/n symmetry. It has been found that the optimized cell suffers a slight deformation in the a-b plane, without significant change of volume.

	a (Å)	b (Å)	c (Å)	β (deg.)	ρ (g/cc)
input	13.757	16.634	19.077	105.289	1.669
optim.	13.808	16.571	19.080	105.299	1.666

Table 3.4. Results of the optimization the monoclinic lattice for PCBM-ODCB. Input cell is from crystallographic data published in [52].

As a final validation for the optimized structure, a numerical simulation of the XRD powder pattern has been performed. The resulting diffraction pattern closely matches the experimental data from the independent measurement performed in [53]; this comparison is displayed in figure 3.11.

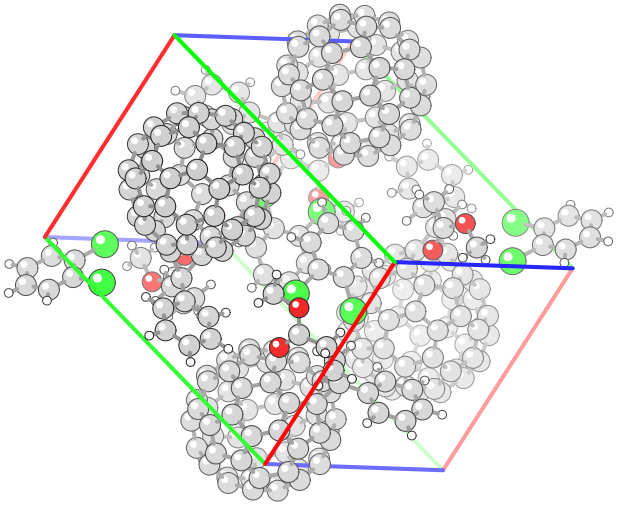

Figure 3.10. Contents of the unit cell for PCBM-ODCB lattice as proposed in [52]. Each unit cell contains four PCBM and four ODCB molecules. Space group: P $2_1/n$.

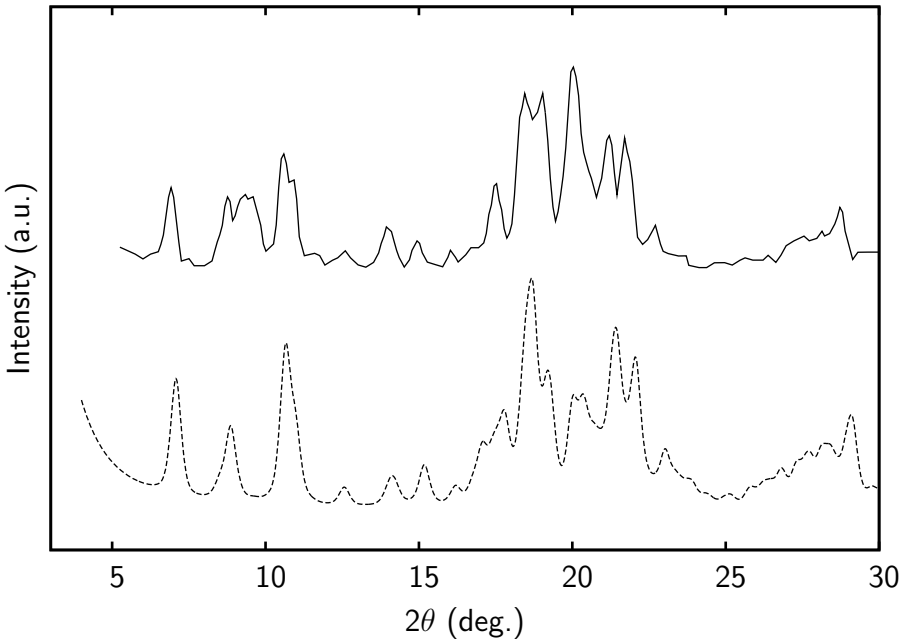

Figure 3.11. Simulated powder XRD profile (dashed line) for the optimized PCBM-ODCB crystal against experimental data (solid line) from [53].

3.3 Summary of the chapter

A heuristic exploration of crystalline packings for PCBM has been performed, including lattice of high and low symmetry.

For high symmetries with one PCBM molecule per unit cell, the simple cubic arrangement shows the lowest energy, with a predicted mass density of 1.445 g/cc, and a first neighbors distance of 10.15, which is only slightly larger than in the case of FCC fullerite. A lower packing energy can be obtained with an hexagonal cell containing a PCBM *dimer*. The PCBM molecules are arranged in a triangular lattice of parameter $a \approx 9.7$ Å; the hexagonal cell has a c parameter compatible with the terraces observed in [57]. In this case, intermolecular interactions between opposing phenyl and ester moieties result into a close packing with a predicted mass density of 1.536 g/cc. The drawback of this model is that it is prone to triclinic deformations, since the contents of the unit cell are not symmetrical under the hexagonal point groups.

Proper low symmetry lattices have also been analyzed, imposing strict space groups on asymmetric unit cells containing a single PCBM molecule. The results show that the hexagonal *dimer* arrangement can be approximated by a proper monoclinic C 2 space group. The simulated diffraction pattern matches the experimental data reported in [57]. However, a complete XRD investigation is required to check higher order reflections and confirm the unit cell proposed in this work. The performance of the packings is presented in figure 3.12.

Finally, the mixed PCBM-ODCB cell proposed in [52] has been found to be energetically stable from our *ab initio* calculation. The cell parameters suffered a minimal distortion, proving that the proposed packing is most likely the correct description of the crystalline morphology of PCBM grown from ODCB.

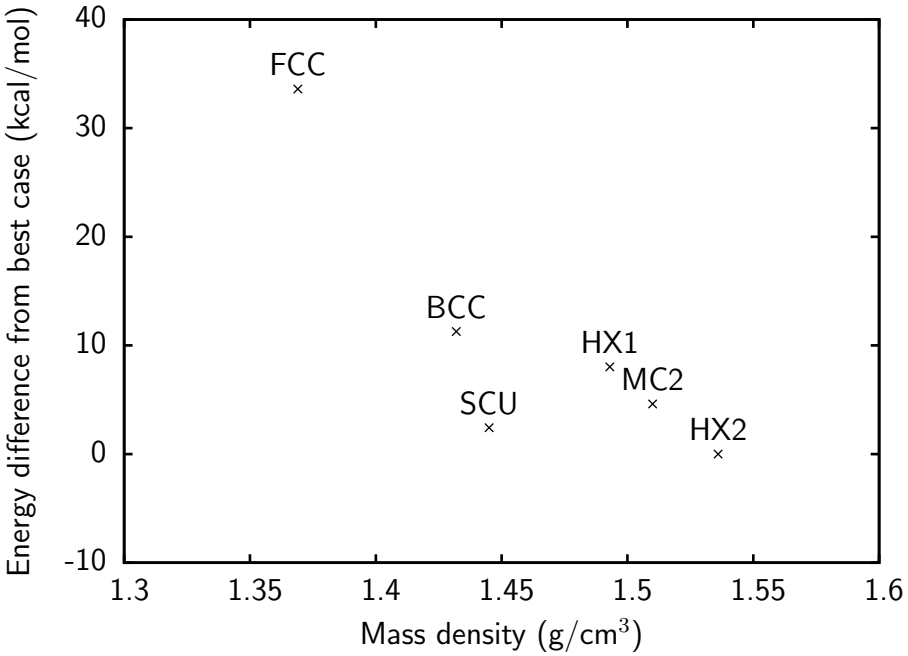

Figure 3.12. Graphical review of the packings proposed: the best performing packing in respect to energy is the hexagonal *dimer* (HX2), followed by the simple cubic (SCU) and the monoclinic C 2 (MC2). The hexagonal *monomer* (HX1), the body centered cubic (BCC) and the face centered cubic (FCC) conclude the ranking. The three hexagonal related packings show the highest mass density for the PCBM crystal.

Conclusions

Photovoltaics represents an important contribution to the development of renewable energy sources. The realization of cost-effective alternatives to the use of fossil fuels entails finding a solution to technical challenges, namely improving the power conversion efficiency and simultaneously lowering the cost of the photovoltaic modules. The research in polymer solar cells tackles these challenges by offering a low cost alternative to the expensive crystalline silicon modules. Presently, the main limitation of polymer solar cells is their low power conversion efficiency. Significant improvement has been obtained in the last years with the adoption of the *bulk heterojunction* concept: an electron donor and an electron acceptor are mixed and cast into a thin film. The resulting bulk is a disordered mix of semicrystalline donor and acceptor domains, for example P3HT and PCBM, respectively. The power conversion efficiency of modules manufactured in this fashion benefits from the significantly high area of interface between donor and acceptor domains, but suffers from the abundance of recombination sites and overall low charge carrier mobility induced by structural disorder. The focus of the present work is to support the development of *ordered* bulk heterojunction manufacturing routes via the *ab initio* assessment of the crystallographic morphology of P3HT and PCBM. It is expected that detailed knowledge about the crystalline morphology will be beneficial to the understanding of crystallization kinetics, and ultimately to the development of supramolecular self-assembly techniques.

Regarding P3HT, the orthorhombic cell inferred by early experimental investigations has been confirmed. In the packing model proposed in this work the primitive cell contains two shifted P3HT backbones; also, it has been found that the alkyl chains suffer no significant interdigitation, due to a non trivial exploiting of available space. The packing model with one P3HT backbone per primitive cell has been rejected, due to its inability to reproduce the experimental XRD profiles. The presence of two different P3HT backbones per cell induces a gemination of both the valence and the conduction bands, causing the calculated optical absorption spectrum to show features which insofar have been otherwise attributed to transitions of excitonic or vibronic character. An *ab initio* investigation in the framework of many-body perturbation theory is being planned to characterize possible excitonic

optical absorption.

Regarding PCBM, a number of high symmetry packing models having one PCBM molecule per primitive cell have been reviewed. In the crystallographic cubic lattice class, the simple cubic centering has shown favorable packing energy but the resulting lattice is prone to significant triclinic deformation once the constraint of fixed cubic symmetry is lifted. The face centered cubic lattice has been rejected due to high packing energy. An hexagonal lattice containing one PCBM molecule per cell results in higher packing energy than the simple cubic lattice, but with a smaller cell volume. The adoption of two PCBM molecules per cell (hexagonal *dimer*) results in the lowest packing energy among the proposed lattices, along with the highest density; this packing is consistent with the six-fold symmetry axis observed in experimental SAED investigations. As an approximation to the hexagonal *dimer* packing, a monoclinic lattice (C 2) has been investigated. In this case, a proper space group has been applied to the asymmetric cell made of one PCBM molecule, resulting into a conventional crystallographic cell containing four PCBM molecules. This particular symmetry results into packing density and energy slightly worse than those obtained with the hexagonal *dimer* packing. A direct collaboration with the research team who demonstrated the feasibility of the crystallization of large quasi-hexagonal PCBM crystals is underway to clearly assess the crystallographic space group of these samples. The determination of the actual packing model of PCBM is a requirement to the realization of an *ab initio* investigation of optical and transport properties of the interface between PCBM and P3HT.

Appendix A

Computational Methods

A.1 *Ab initio* calculations

This section serves as a technical reference for the *ab initio* methods used in the calculations of the optimized crystalline structures and electronic properties of P3HT and PCBM. The calculations have been performed with the CRYSTAL09 software, a program for the *ab initio* quantum-mechanical study of crystalline solids developed by the Theoretical Chemistry Group of the University of Turin. The CRYSTAL09 code performs Kohn-Sham (KS) density functional theory (DFT) calculations using atom-centered Gaussian basis sets; furthermore it allows to minimize the electron energy of the crystalline primitive cell with respect to the atomic positions and cell parameters using analytical gradients and numerical Laplacian, exploiting both the translational and point group symmetry of the cell.

The following subsections detail the steps undertaken in the simulation, in particular the solving of the self consistent field (SCF) electronic problem, the implementation of London-type empirical dispersion interactions (van der Waals) and the optimization of the geometrical degrees of freedom. For further details about the software implementation of these methods we refer to the manual of CRYSTAL09 and the references cited therein.

A.1.1 Electronic SCF problem

Kohn-Sham Hamiltonian

The ground state energy of a N-electron system in the field of an external ionic potential v_{ext} is obtained by applying the KS-DFT method to the crystalline system. The electronic energy is evaluated from the KS functional:

$$E_{KS}[\{\phi_i\}] = T_{KS}[\rho] + \int \rho(\mathbf{r}) v_{ext}(\mathbf{r})\, \mathrm{d}\mathbf{r} + \frac{1}{2} \iint \frac{\rho(\mathbf{r})\rho(\mathbf{r}')}{|\mathbf{r}-\mathbf{r}'|}\, \mathrm{d}\mathbf{r}\mathrm{d}\mathbf{r}' + E_{XC}[\rho] \tag{A.1}$$

$$\rho(\mathbf{r}) = \sum_{i=1}^{N/2} |\phi_i|^2 \qquad T_{KS}[\rho] = -\frac{1}{2} \sum_{i=1}^{N/2} \phi_i^* \nabla^2 \phi_i \tag{A.2}$$

where both the density ρ and the kinetic energy T_{KS} are promptly calculated over the KS orbitals $\{\phi_i\}$; E_{XC} is the exchange-correlation functional, whose choice fixes the KS Hamiltonian. The KS orbitals are obtained from the self-consistent solution of the KS eigenvalue equations by iterative methods:

$$\mathcal{F}_{KS}(\mathbf{r})\, \phi_i(\mathbf{r}) = \varepsilon_i\, \phi_i(\mathbf{r}) \qquad i = 1, \cdots, N/2 \tag{A.3}$$

$$\mathcal{F}_{KS} = -\frac{1}{2}\nabla^2 + v_{ext}(\mathbf{r}) + \int \frac{\rho(\mathbf{r}')}{|\mathbf{r}-\mathbf{r}'|}\, \mathrm{d}\mathbf{r}' + v_{XC}(\mathbf{r}) \qquad v_{XC}(\mathbf{r}) = \frac{\delta E_{XC}[\rho]}{\delta \rho} \tag{A.4}$$

The KS orbitals do not strictly correspond to physical single-particle eigenstates, however, a rigorous perturbative treatment [62] shows that Kohn-Sham eigenvalue differences are a well-defined approximation to electronic excitation energies.

The iterative solution of the KS equations A.3 provides KS eigenvalues and eigenstates and allows to calculate the electronic energy A.1. All these quantities are parametric functions of the set of atomic coordinates $\mathbf{d}_\mu$ and cell parameters (where applicable). Note that the iterative process for solving the KS equations can present convergence problems whose solution can require special numerical tricks. The complete reference for the numerical implementation of the self-consistent iterative cycles is included in CRYSTAL manual.

Pseudopotential and gaussian basis set

Due to the high number of atoms present in the crystalline systems subject to our analysis, an all-electron calculation was not computationally feasible. Durand effective core pseudopotentials (ECP) were used for the non-hydrogen atoms to reduce the all-electron problem to valence electrons only. The pseudopotential associated to a particular ion is:

$$W_{ps}(r) = -\frac{Z - Z_{\text{core}}}{r} + \sum_l w_l(r)\mathcal{P}_l \tag{A.5}$$

$$w_l(r) = \exp(-\alpha_l r^2) \sum_{k=1}^{M} C_k r^{n_k} \tag{A.6}$$

$$\mathcal{P}_l = \sum_{m=-l}^{+l} |Y_l^m\rangle \langle Y_l^m| \tag{A.7}$$

The first term in the right side A.5 represents the screened Coulomb interaction with the nucleus, while the second term is an appropriate repulsive potential with a different shape $w_l(r)$, depending on the value of the angular moment in the subspace selected by the projector $\mathcal{P}_l$. The values of the α_l, C_k and n_k parameters are hardcoded into the CRYSTAL software, and have been published in [63, 64]. A pseudopotential specific basis set was used to represent the (pseudo-)wavefunctions of valence electrons for each atom in the cell.

CRYSTAL performs *ab initio* calculations on periodic systems within the linear combination of atomic orbitals approximation. That is, the crystalline orbitals ψ are treated as linear combinations of Bloch functions ϕ, defined in terms of local

functions φ, hereafter indicated as atomic orbitals.

$$\psi_i(\mathbf{r};\mathbf{k}) = \sum_\mu a_{\mu,i}(\mathbf{k})\,\phi_\mu(\mathbf{r};\mathbf{k}) \tag{A.8}$$

$$\phi_\mu(\mathbf{r};\mathbf{k}) = \sum_{\mathbf{t}_m} \varphi_\mu(\mathbf{r}-\mathbf{d}_\mu-\mathbf{t}_m)\,\mathrm{e}^{\mathrm{i}\mathbf{k}\cdot\mathbf{t}_m} \tag{A.9}$$

where $\mathbf{d}_\mu$ is the position of the μ-th nucleus in the primitive cell, and $\mathbf{t}_m$ spans the set of direct lattice vectors. The localized functions φ are expressed as linear combinations of a basis set of Gaussian type functions χ^{GTF}, with suitable coefficients d_j and exponents α_j:

$$\varphi_\mu(\mathbf{r}-\mathbf{d}_\mu-\mathbf{t}) = \sum_j d_j\,\chi^{GTF}(\alpha_j;\mathbf{r}-\mathbf{d}_\mu-\mathbf{t}) \tag{A.10}$$

$$\chi^{GTF}(\alpha;(x,y,z)) = x^l y^m z^n\,\exp(-\alpha(x^2+y^2+z^2)) \tag{A.11}$$

The advantage ot the description in terms of cartesian Gaussian functions is that they represent a complete basis set, and the corresponding monoelectronic and bielectronic integrals involved in the calculations are completely analytical.

The wavefunctions of valence electrons are described by a linear combination of two GTFs for each atomic orbital in the inner valence shell and one GTF for each atomic orbital in the outer valence shell. As an example we explicitly work out the case of the carbon atom ([He] $2s^2\ 2p^2$). The core electron shell 1s is ruled out by the use of the appropriate pseudopotential. The inner valence contains the 2s and 2p shells, while the outer valence contains the 3s,3p,3d shells. Thus, the inner valence shell is described with a linear combination of one s-type and three p-type atomic orbitals, while the outer valence is described with one s-type, three p-type and five d-type atomic orbitals:

$$\text{I.V.}\ \begin{cases} \varphi_{C,2s}(\mathbf{r}) = & \left[d^{(0)}_{C,2s}\exp(-\alpha^{(0)}_{C,2sp}r^2) + d^{(1)}_{C,2s}\exp(-\alpha^{(1)}_{C,2sp}r^2)\right]Y^{m=0}_{l=0} \\ \varphi_{C,2p}(\mathbf{r}) = & r\left[d^{(0)}_{C,2p}\exp(-\alpha^{(0)}_{C,2sp}r^2) + d^{(1)}_{C,2p}\exp(-\alpha^{(1)}_{C,2sp}r^2)\right]Y^{m}_{l=1} \end{cases} \tag{A.12}$$

$$\text{O.V.}\ \begin{cases} \varphi_{C,3s}(\mathbf{r}) = & \left[\exp(-\alpha_{C,3sp}r^2)\right]Y^{m=0}_{l=0} \\ \varphi_{C,3p}(\mathbf{r}) = & r\left[\exp(-\alpha_{C,3sp}r^2)\right]Y^{m}_{l=1} \\ \varphi_{C,3d}(\mathbf{r}) = & r^2\left[\exp(-\alpha_{C,3d}r^2)\right]Y^{m}_{l=2} \end{cases} \tag{A.13}$$

The angular dependence is included into the spherical harmonics Y^m_l, where it is implied that the index m runs over the range $\{-l,\cdots,+l\}$. The actual exponents and coefficients are reported in table A.1. For computational convenience the gaussian exponents in s-p shells are assumed to be equal. A plot of carbon inner valence 2s-type and 2p-type atomic orbitals (eqn. A.12) is presented in figure A.1.

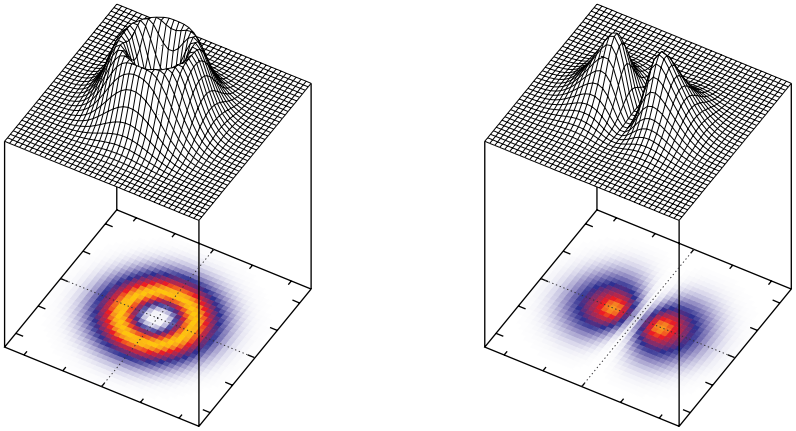

Figure A.1. Plot of the squared modulus of eqn. A.12 in the xy plane. Depending on the angular component a s-type function (left plot) or a p-type function (right plot) is obtained. The corresponding wavefunctions are the result of a contraction of two GTFs with the coefficients and exponents reported in tab. A.1; they are used as a representation of the inner valence sp shell of carbon atoms under the action of the Durand pseudopotential.

	inner valence			outer valence	
#	$\alpha_{C,2sp}$	$d_{C,2s}$	$d_{C,2p}$	$\alpha_{C,3sp}$	$\alpha_{C,3d}$
(0)	2.927124	-0.146932	0.165474	0.2	0.8
(1)	0.659924	0.416847	0.487652	–	–

Table A.1. Numerical parameters used to model inner and outer valence shells for carbon atoms described by Durand pseudopotential.

Exchange and correlation functionals

The E_{XC} functional contains the energy corrections due to non-classical interactions in a many-body quantum system, which include exchange and correlation effects. These corrections have been calculated numerically in the case of an homogeneous electron gas. These results have been adapted to the non-homogeneous electron gas by approximating it as a locally homogeneous system: this approximation goes

under the name of local density approximation (LDA). An improvement over LDA is to include corrections dependent on the density gradient to reproduce short range electron correlations: this approximation is called generalized gradient approximation (GGA). The resulting functionals are typically better performing than LDA in energetic and geometrical properties of systems in which the electron gas has strong localization, and, in general, they show an improved description of systems in which hydrogen bonds are present. The GGA functionals thus represent a natural choice for the modeling of molecular crystals.

For the exchange part of E_{XC} we chose the Becke [65] functional, while for the correlation part we chose the Lee, Yang and Parr [66] functional. The combined exchange-correlation functional is known as BLYP. This choice for the exchange-correlation functional is corroborated by the good performance in *ab initio* simulation of water as well as other molecular systems where weak intermolecular bonds are present [67, 68]. In the preliminar calculations for the P3HT system the B3LYP functional was also used. This particular functional integrates BLYP with an exchange energy which is contributed by an exact Hartree-Fock calculation. The resulting hybrid functional, being optimized against experimental atomic properties, is known to improve the estimation of the energy of excited states, in particular of the energy gap, and is thus a popular choice in theoretical chemistry. However, the *ab initio* estimation of the energy gap was not our primary goal; furthermore in systems composed of a large number of atoms the computational cost of the evaluation of Hartree-Fock exchange energy outweights the accuracy in the estimation of excited states energies. Where required, the energy gap was corrected by means of a scissor operator applied over the eigenvalues obtained with BLYP functional. For further details regarding the theoretic and computational aspects of DFT methods we refer to [69].

Van der Waals interactions

A general drawback of all common GGA functionals is that they cannot take into account the long-range electron correlations that are due to van der Waals dispersive forces. In CRYSTAL09 a modified KS-DFT energy functional is available to include such long-range interactions via a semi-empirical expression for the corresponding energy contribution:

$$E_{KS-vdW} = E_{KS} - s_6 \frac{1}{2} \sum_{i \neq j} \frac{C_6^{ij}}{R_{ij}^6} f_{dmp}(R_{ij}) \tag{A.14}$$

$$f_{dmp}(R_{ij}) = \frac{1}{1 + \exp\left(-d\left(R_{ij}/R_r - 1\right)\right)} \qquad R_{ij} = |\mathbf{R}_i - \mathbf{R}_j| \tag{A.15}$$

In equation A.14 the energy due to the dispersion forces is evaluated as a sum over the ion pairs in the primitive cell; each pair contributes a R_{ij}^{-6} term, with short range

cutoff given by the damping function f_{dmp}, in which the parameter R_r represent the sum of the van der Waals radii of the two ions. The method has been presented in [25], where the parameters s_6, C_6^{ij} and d are estimated for several elements by fitting the calculated interaction energies against experimental data. In this framework, van der Waals interactions act as additional forces applied to the nuclei; they are analytically computed during the geometry optimization.

A.1.2 Geometry optimization

The geometry optimization process consists in the relaxation of some of the geometrical degrees of freedom of the system. The complete set of geometrical degrees of freedom is defined as a maximal set of independent parameters which can describe the spatial positions of atoms belonging to a given crystalline lattice. The CRYSTAL code allows to relax the complete set as well as a specific subset of the complete set of geometrical degrees of freedom, *e.g.* forcing a fixed-volume constraint on the primitive cell, or optimizing the internal coordinates of the atoms having the cell fixed. Depending on required space symmetry and any other geometrical constraint, the cardinality of the optimized subset of geometrical parameters (N_{opt}) is then typically less than ($P_{cell} + N_{at}$), where P_{cell} is the number of free parameters for the Bravais lattice and N_{at} is the number independent interatomic coordinates in the primitive cell.

In the geometry optimization the motion of nuclei[1] follows quasi-Newtonian dynamics within the Broyden-Fletcher-Goldfarb-Shanno method. The Hellmann-Feynman forces acting on each nucleus are evaluated *analytically* from the expression of the KS-DFT energy functional (eqn. A.1) even with the inclusion of van der Waals interactions (eqn. A.14); this allows the system to efficiently relax towards the optimal configuration, in which the forces vanish and the Hessian matrix of second derivatives of energy over the degrees of freedom is positive definite.

[1]Formally this should read as: "the evolution of the relaxed subset of parameters".

A.1.3 Dielectric function calculation

Dielectric functions have calculated with the Quantum Espresso software suite, an open source collection of code for the implementation of KS-DFT methods with atomic pseudopotentials and plane wave basis set. The electronic wavefunctions have been computed with fixed ionic geometry (provided by the optimization performed by the CRYSTAL code). For the exchange-correlation functional, the BLYP has been used for consistency with CRYSTAL calculations; the main difference being the adoption of a different pseudopotential/basis set. In this case Troullier-Martins pseudopotential are used, along with a plane wave basis set with a cutoff at 60 Rydberg, which allows for accurate representation of the electronic wavefunctions.

For incident light of frequency ω and polarization direction $\hat{e}$, the macroscopic transverse dielectric function can be approximated by the Drude-Lorentz expression:

$$\epsilon(\hat{e};\omega) = 1 + \omega_p^2 \sum_{c,v} \sum_{\mathbf{k}} \frac{f_{v\mathbf{k}}^{c\mathbf{k}}(\hat{e})}{[(\omega_{c\mathbf{k}} - \omega_{v\mathbf{k}})^2 - \omega^2] - i\ \gamma\omega} \tag{A.16}$$

where $\omega_p = \frac{4\pi n e^2}{m}$ is the free-electron plasma frequency and γ a is finite energy width ($\hbar\gamma = 0.2$ eV in our calculations) that takes into account the non-monochromaticity of the incident light and the finite lifetime of the excited levels of the system; $f_{v\mathbf{k}}^{c\mathbf{k}}(\hat{e})$ is the oscillator strength of the $|\Psi_{v\mathbf{k}}\rangle \rightarrow |\Psi_{c\mathbf{k}}\rangle$ transition between valence and conduction crystalline orbitals of energies $\hbar\omega_{v,\mathbf{k}}$ and $\hbar\omega_{c,\mathbf{k}}$, respectively. The expression of the oscillator strength is

$$f_{v\mathbf{k}}^{c\mathbf{k}}(\hat{e}) = \frac{2}{\hbar m N V} \frac{|M_{c,v}(\hat{e},\mathbf{k})|^2}{\omega_{c\mathbf{k}} - \omega_{v\mathbf{k}}} \tag{A.17}$$

where V is the crystal volume, N the number of electrons per unit volume and $M_{c,v}(\hat{e},\mathbf{k}) = \langle \Psi_{c\mathbf{k}} \,|\, \hat{e}\cdot\mathbf{p} \,|\, \Psi_{v\mathbf{k}} \rangle$ is the matrix element of the electromagnetic pertubation for a one-electron excitation from valence to conduction.

A.2 XRD spectra simulation

This section provides a technical reference for a basic method used to simulate powder XRD $\theta - 2\theta$ profiles. In the following subsections, the fundamentals of x-ray diffraction are briefly derived, along with the relevant geometric definitions used in diffractometry. A simulation algorithm for the calculation of the powder XRD profile for general crystalline compounds is then devised.

A.2.1 Diffractometry

X-ray diffractometry (XRD) is a technique used to characterize the crystalline morphology of solid state compounds. Diffraction patterns are observed when electromagnetic radiation scatters on periodic structures whose length scale matches the wavelength of the radiation. The inter-atomic distances in condensed matter typically lie in 1.5–4.0 Å range; photons with such wavelengths have energies comprised in the 3–8 keV range, and thus belong to the x-ray portion of electromagnetic spectrum. An x-ray diffractometer includes a radiation source (an x-ray tube or a

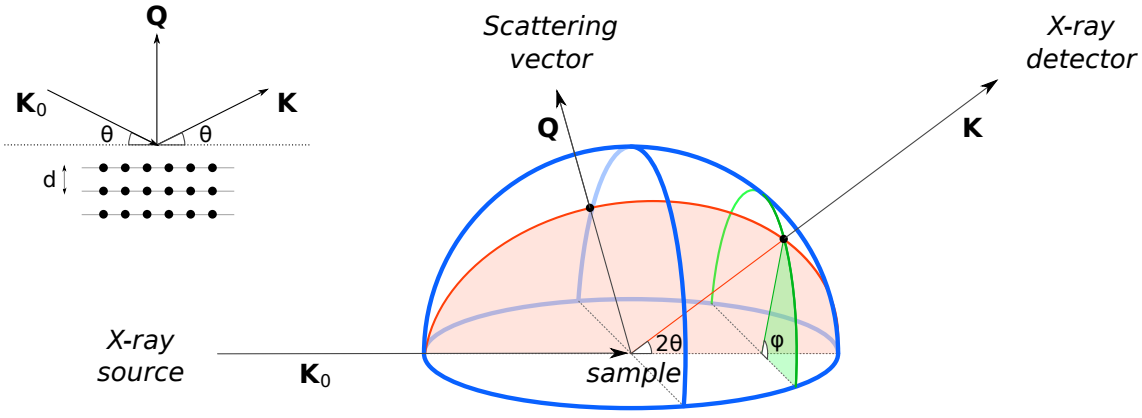

Figure A.2. Basic geometry in x-ray diffractometers.

synchrotron radiation beam), a sample holder and an appropriate detector. These elements allow the experimenter to record the diffraction pattern, *i.e.*, the intensity of x-ray radiation I_d picked up by the detector, whose position is varied by scanning the surface of the ideal sphere centered on the sample.

$$I_d = I(\theta,\phi)$$

The dependence of I_d on the angular coordinates θ and ϕ allows to reconstruct the full diffraction profile, which in turn bears information about the crystalline morphology of the sample specimen. A full diffraction profile can be summarized in a set of diffraction peaks characterized by angular position, intensity and shape. The following subsections briefly develop the fundamentals of XRD analysis.

A.2.2 Coherent Thomson scattering

X-rays of energy in the 3–8 keV range interact with electrons in matter in three different processes:

- Thomson scattering (elastic)
- Compton scattering (inelastic)
- Photoionization (inelastic)

XRD patterns are due to the elastic Thomson scattering, a process in which a charge oscillates as a dipole at the same frequency of the incoming radiation, with the oscillating dipole becoming the source of the scattered radiation. Since there is no change in the frequency of the photons involved, the process is described as an elastic scattering.

According to Thomson's derivation, the intensity of the beam scattered by *a single* electron from unpolarized incoming radiation I_0 is:

$$I_e(\mathbf{R}) = I_0 \frac{r_e^2}{R^2} \frac{1 + \cos^2 2\theta}{2} \tag{A.18}$$

where $r_e = e^2/4\pi\epsilon_0 m_e c^2$ is the classical radius of the electron, and $\mathbf{R}$ is the vector defining the position of the observer as viewed from the sample holder; the scattering angle 2θ is defined as the angle between the incoming ($\mathbf{K}_0$) and the scattered ($\mathbf{K}$) wave vectors:

$$2\theta = \arccos \frac{(\mathbf{K} \cdot \mathbf{K}_0)}{K K_0} \tag{A.19}$$

Due to the small value of r_e ($\approx 3 \times 10^{-15}$ m) the amount of radiation scattered by a single electron in a specimen examined within a typical diffractometer ($R \approx 0.3$ m) arrangement is negligible:

$$\frac{I_e(\mathbf{R})}{I_0} \approx 10^{-28}$$

It must be emphasized that Thomson scattering occurs not only from electrons, but also from the positively charged nuclei. However, in the case of an atomic nucleus,

the classical radius r_{nucl} is smaller than r_e due to the difference in mass between the nucleus and the electron. At best, for a proton:

$$r_{nucl} = r_{pr} = r_e \frac{m_e}{m_{pr}} \approx \frac{r_e}{1840}$$

It follows that the scattered radiation intensity for nuclei is at least 10^6 times smaller than in the case of electrons, and it is thus neglected.

The fundamental point which enables the detection of scattered radiation (and which justifies the use of XRD techniques for crystallographic analysis) is that a crystal is composed of a periodic array of scatterers. For selected directions of the scattered radiation a coherent interference can be observed between electrons belonging to families of parallel crystal planes. The gain in intensity for a coherent scattering of N centers is of order N^2; given that crystals are macroscopic objects, this gain is sufficiently strong to counteract the negligible cross section of the scattering from a single electron.

To observe a diffraction peak it is necessary (but not sufficient) that the following equation holds:

$$2d_{hkl} \sin\theta_B = \lambda \tag{A.20}$$

where d_{hkl} is the interplanar distance for Miller indexes hkl, θ_B is half the scattering angle and λ is the wavelength of the incoming radiation. Eqn. A.20 is called Bragg equation, and θ_B Bragg angle. A more general formulation can be derived with the introduction of the scattering vector:

$$\mathbf{Q} = \mathbf{K} - \mathbf{K}_0 \tag{A.21}$$

From eqn. A.20 and the construction of $\mathbf{Q}$ for an elastic scattering follows:

$$|\mathbf{G}_{hkl}| = \frac{2\pi}{d_{hkl}} = \frac{4\pi}{\lambda} \sin\theta_B = |\mathbf{K}_0| 2 \sin\theta_B = |\mathbf{Q}| \tag{A.22}$$

where $\mathbf{G}_{hkl} = h\mathbf{g}_1 + k\mathbf{g}_2 + l\mathbf{g}_3$ is the reciprocal lattice vector for Miller indexes hkl. Considering that x-rays are reflected by the $\{hkl\}$ family of planes as in a mirror, it can be deduced that the scattering vector must be normal to the reflecting planes, so that eqn. A.22 is to be replaced by the stronger condition:

$$\mathbf{G}_{hkl} = \mathbf{Q} \tag{A.23}$$

To summarize: the scattering vector $\mathbf{Q}$ is fixed by the position of the detector relative to the source axis $\hat{\mathbf{K}}_0$ and by the wavelength of the radiation, while the set of reciprocal vectors $\mathbf{G}_{hkl}$ is determined by the type and orientation of the crystal lattice in the sample; a diffraction peak *can be observed* if the scattering vector $\mathbf{Q}$ coincides with a reciprocal vector $\mathbf{G}_{hkl}$ for some values of the Miller indexes hkl.

Powder samples

Insofar, only monocrystalline samples have been considered. In general, experimental specimens are composed of multiple crystalline domains, which can be statistically varied with respect to type, size and orientation. In the particular case of a crystalline powder, the grain distribution is isotropic in orientation, with each grain still being sufficiently macroscopic to scatter a detectable portion of the incoming radiation. Due to the superposition of the radiation scattered from grains with different orientation, the diffraction pattern recorded from a powder sample shows peaks uniformly smeared to form rings whose plane is perpendicular to the source axis $\hat{\mathbf{K}}_0$. In this case, due to the rotational symmetry around the source axis, the detector need not to perform a scan over the longitudinal angle ϕ, but only over the latitudinal angle θ. The resulting data can then be conveniently represented as a $I(2\theta)$ or $I(|\mathbf{Q}|)$ dependence. However, this practical simplification comes at the expense of loss of information regarding the $\mathbf{G}_{hkl}$ star, since only $|\mathbf{G}_{hkl}|$ data are recorded. This can induce difficulties in the indexing of peaks originating from low symmetry lattices.

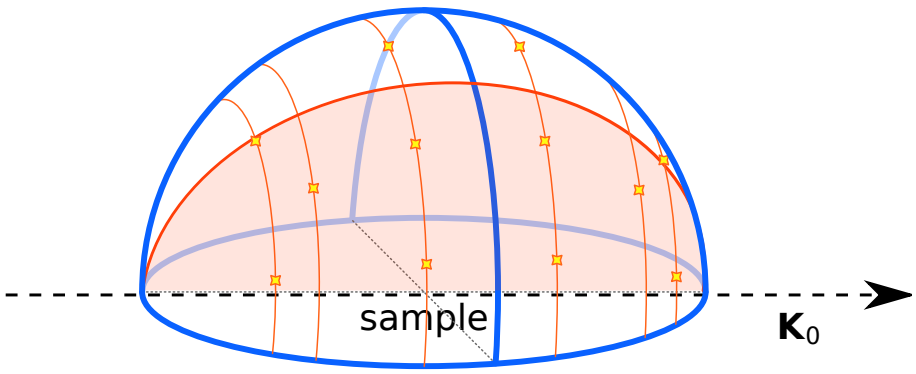

Figure A.3. Powder x-ray diffraction geometry. The randomness in the spatial orientation of the crystalline grains causes the diffraction peaks to be smeared into rings concentric with the $\mathbf{K}_0$ axis. The ring diffraction pattern can be picked up by the detector via a single scan over the θ angle.

A.2.3 Intensity of diffracted peaks

Structure factor

The intensity of a diffraction peak can be evaluated by noticing that in the Fraunhofer approximation the total (complex) amplitude of the field scattered from a charge distribution is proportional to the sum of the field from each scatterer, each weighted with a complex phase factor. This sum is called *structure factor* ($\mathcal{F}$), spans the contents of the primitive cell and is dependent on the scattering vector $\mathbf{Q}$.

$$\mathcal{F}(\mathbf{Q}) = \int_{p.c.} \rho_e(\mathbf{r}) \exp(-\mathrm{i}\mathbf{Q}\cdot\mathbf{r})\,\mathrm{d}\mathbf{r} \tag{A.24}$$

The structure factor can be evaluated by taking the Fourier transform of the spatial density of the electrons in the unit cell, if such data is available. If not, a reasonable approximation is to consider the electrons as localized around each atom, to split the integral into the sum of a finite number (N_{at}) of atomic contributions:

$$\rho_e(\mathbf{r}) \approx \sum_{n=1}^{N_{at}} \rho_{e,n}(\mathbf{r}-\mathbf{d}_n) \tag{A.25}$$

$$\mathcal{F}(\mathbf{Q}) \approx \sum_{n=1}^{N_{at}} \int \rho_{e,n}(\tau) \exp(-\mathrm{i}\mathbf{Q}\cdot(\tau+\mathbf{d}_n))\,\mathrm{d}\tau \tag{A.26}$$

where $\rho_{e,n}$ and $\mathbf{d}_n$ are the reference electronic density and the position of the n-th atom in the primitive cell, respectively, while $\tau = \mathbf{r} - \mathbf{d}_n$ is a convenience variable. Integrating eqn. A.26 in τ, the following equations are obtained:

$$f_n(\mathbf{Q}) = \int \rho_{e,n}(\tau) \exp(-\mathrm{i}\mathbf{Q}\cdot\tau)\,\mathrm{d}\tau \tag{A.27}$$

$$\mathcal{F}(\mathbf{Q}) \approx \sum_{n=1}^{N_{at}} f_n \exp(-\mathrm{i}\mathbf{Q}\cdot\mathbf{d}_n) \tag{A.28}$$

where the atomic form factors f_n are tabulated real-valued functions of $|\mathbf{Q}|$ and of the atomic number (International Tables for Crystallography, vol.C chapter 6.1). Given a particular tern of Miller indexes, the relevant structure factor is:

$$\mathcal{F}(hkl) \approx \sum_{n=1}^{N_{at}} f_n(|\mathbf{G}_{hkl}|) \exp(-\mathrm{i}\mathbf{G}_{hkl}\cdot\mathbf{d}_n) \tag{A.29}$$

Geometry, Lorentz and Polarization factors

For powder samples, the smearing of diffraction peaks over circular rings introduces a further angular dependency in the intensity. The intensity picked up by the detector is inversely proportional to the circumference of the ring, causing a dilution of intensity by $1/\sin 2\theta$. The intensity must also be directly proportional to the fraction of crystallites that are in the correct position to reflect, which scales as $\cos\theta$. The combination of these effects is called *geometric factor*:

$$G(\theta) = \frac{\cos\theta}{\sin 2\theta} \propto \frac{1}{\sin\theta} \tag{A.30}$$

The *Lorentz factor* accounts for angular dependence in the radiation picked up by the detector during the scan over θ. In a diffractometer the intensity picked up by the detector must be directly proportional to the time of exposure, which in turn is inversely proportional to the relative velocity between the detector and the "image" of the peak during the $\theta - 2\theta$ scan. Elementary geometry considerations show that this velocity scales as $\sin\theta\cos\theta$:

$$L(\theta) = \frac{1}{\sin\theta\cos\theta} \propto \frac{1}{\sin 2\theta} \tag{A.31}$$

The last angular dependence considered here regards the polarization. This dependence has already been shown in eqn. A.18 for the Thomson scattering from an unpolarized beam. This angular dependence is called *polarization factor*:

$$P(\theta) = \frac{1 - \cos^2 2\theta}{2} \propto (1 - \cos^2 2\theta) \tag{A.32}$$

These factors are to be combined together to give:

$$GLP(\theta) = \frac{1 - \cos^2 2\theta}{\sin^2\theta\cos\theta} \tag{A.33}$$

valid for powder samples in the Debye-Scherrer geometry arrangement (International Tables of Crystallography, vol. C, table 6.2.1.1).

Overall, the intensity of the peaks can be estimated as:

$$I_d(hkl) \propto GLP(\theta_B(hkl))\,|\mathcal{F}(hkl)|^2 \tag{A.34}$$

A.2.4 Simulation algorithm

To simulate a complete XRD powder $\theta - 2\theta$ spectrum for a crystalline lattice, the following algorithm has been used:

1. The reciprocal lattice vectors $\mathbf{G}_{hkl}$ are generated from the parameters of the primitive cell
2. For each hkl tern with $|\mathbf{G}_{hkl}| \leq \frac{4\pi}{\lambda}$:
   (a) The angle of reflection $\theta_B(hkl)$ is obtained from either A.20 or A.22.
   (b) The intensity $I_d(hkl)$ of the peak is estimated from A.34
   (c) A pseudo-Voigt line profile[2] is computed for the hkl reflection:

$$\varphi_{hkl}(\theta) = I_d(hkl)\left(\exp\left(-\ln 2\left(\frac{\theta-\theta_B}{w}\right)^2\right) + \frac{1}{1+\left(\frac{\theta-\theta_B}{w}\right)^2}\right) \tag{A.35}$$

   where w is a reasonable constant linewidth.
3. The complete diffraction profile is obtained by direct summation of the line profiles obtained for each hkl.

$$I_{sim}(\theta) = \sum_{hkl} \varphi_{hkl}(\theta) \tag{A.36}$$

[2]With 50% mixing between Lorentzian and Gaussian shapes.

Bibliography

[1] Green, M. A.
Photovoltaics: Coming of age.
In *Photovoltaic Specialists Conference, 1990., Conference Record of the Twenty First IEEE*, pages 1–8 (1990).

[2] Becquerel, E.
Recherches sur les effets de la radiation chimique de la lumière solaire, au moyen des courants électriques.
Comptes Rendus des Séances Hebdomadaires, 9:145 (1839).

[3] Becquerel, E.
Mémoire sur les effets électriques produits sous l'influence des rayons solaires.
Comptes Rendus des Séances Hebdomadaires, 9:561 (1839).

[4] Adams, W. G. and Day, R. E.
The Action of Light on Selenium.
Proceedings of the Royal Society of London (1854-1905), 25(-1):113 (1876).
doi:10.1098/rspl.1876.0024.

[5] Green, M. A.
Photovoltaic principles.
Physica E: Low-dimensional Systems and Nanostructures, 14(1-2):11 (2002).
doi:10.1016/S1386-9477(02)00354-5.

[6] Ohl, R. S.
Light-sensitive electric device including silicon (1948).

[7] Chapin, D. M. *et al.*
A New Silicon p-n Junction Photocell for Converting Solar Radiation into Electrical Power.
Journal of Applied Physics, 25(5):676 (1954).
doi:10.1063/1.1721711.

[8] King, R. R. *et al.*
40% efficient metamorphic GaInP/GaInAs/Ge multijunction solar cells.
Applied Physics Letters, 90(18):183516 (2007).
doi:10.1063/1.2734507.

[9] Würfel, P.
Physics of solar cells.
Wiley-VCH (2005).
ISBN 3-527-40428-7.

[10] Sera, D. *et al.*
PV panel model based on datasheet values.
In *IEEE International Symposium on Industrial Electronics*, 4, pages 2392–2396 (2007).

[11] Lynn, P. A.
Electricity from Sunlight: An Introduction to Photovoltaics.
John Wiley and Sons (2010).
ISBN 978-0-470-74560-1.

[12] Goetzberger, A. and Hoffmann, V.
Photovoltaic solar energy generation.
Springer Series in optical sciences. Springer (2005).
ISBN 3-540-23676-7.

[13] Green, M. A. *et al.*
Solar cell efficiency tables (version 36).
Progress in Photovoltaics: Research and Applications, 18(5):n/a (2010).
doi:10.1002/pip.1021.

[14] Gao, F. *et al.*
A new heteroleptic ruthenium sensitizer enhances the absorptivity of mesoporous titania film for a high efficiency dye-sensitized solar cell.
Chemical communications, pages 2635–2637 (2008).
doi:10.1039/b802909a.

[15] Sariciftci, N. S. and Hoppe, H.
Polymer Solar Cells, volume 214, chapter 1, pages 1–86.
Springer, advances i edition (2008).
ISBN 978-3-540-69452-6.
doi:10.1007/12_2007_121.

[16] Hou, J. *et al.*

Synthesis of a low band gap polymer and its application in highly efficient polymer solar cells.
Journal of the American Chemical Society, 131(43):15586 (2009).
doi:10.1021/ja9064975.

[17] Yue, S. *et al.*
Intermolecular Association and Supramolecular Organization in Dilute Solution. 1. Regioregular Poly(3-dodecylthiophene).
Macromolecules, 29(3):933 (1996).
doi:10.1021/ma951008+.

[18] Winokur, M. J. *et al.*
Structural evolution in iodine-doped poly(3-alkylthiophenes).
Macromolecules, 24(13):3812 (1991).
doi:10.1021/ma00013a011.

[19] McCullough, R. D. *et al.*
Self-orienting head-to-tail poly(3-alkylthiophenes): new insights on structure-property relationships in conducting polymers.
Journal of the American Chemical Society, 115(11):4910 (1993).
doi:10.1021/ja00064a070.

[20] McCullough, R. D.
The first synthesis and new properties of regioregular, head-to-tail coupled polythiophenes.
Synthetic Metals, 69(1-3):279 (1995).
doi:10.1016/0379-6779(94)02449-9.

[21] Kline, R. *et al.*
Controlling the Field-Effect Mobility of Regioregular Polythiophene by Changing the Molecular Weight.
Advanced Materials, 15(18):1519 (2003).
doi:10.1002/adma.200305275.

[22] Goh, C. *et al.*
Molecular-weight-dependent mobilities in regioregular poly(3-hexyl-thiophene) diodes.
Applied Physics Letters, 86(12):122110 (2005).
doi:10.1063/1.1891301.

[23] Kline, R. J. *et al.*
Dependence of Regioregular Poly(3-hexylthiophene) Film Morphology and Field-Effect Mobility on Molecular Weight.

Macromolecules, 38(8):3312 (2005).
doi:10.1021/ma047415f.

[24] Brinkmann, M. and Rannou, P.
Molecular Weight Dependence of Chain Packing and Semicrystalline Structure in Oriented Films of Regioregular Poly(3-hexylthiophene) Revealed by High-Resolution Transmission Electron Microscopy.
Macromolecules, 42(4):1125 (2009).
doi:10.1021/ma8023415.

[25] Grimme, S.
Semiempirical GGA-type density functional constructed with a long-range dispersion correction.
Journal of computational chemistry, 27(15):1787 (2006).
doi:10.1002/jcc.20495.

[26] Canetti, M. *et al.*
Structural investigation on bulk poly(3-hexylthiophene): Combined SAXS, WAXD, and AFM studies.
European Polymer Journal, 45(9):2572 (2009).
doi:10.1016/j.eurpolymj.2009.06.012.

[27] Joshi, S. *et al.*
X-ray structural and crystallinity studies of low and high molecular weight poly(3-hexylthiophene).
Physica Status Solidi (a), 205(3):488 (2008).
doi:10.1002/pssa.200723423.

[28] Joshi, S. *et al.*
Thickness Dependence of the Crystalline Structure and Hole Mobility in Thin Films of Low Molecular Weight Poly(3-hexylthiophene).
Macromolecules, 41(18):6800 (2008).
doi:10.1021/ma702802x.

[29] Brinkmann, M. and Rannou, P.
Effect of Molecular Weight on the Structure and Morphology of Oriented Thin Films of Regioregular Poly(3-hexylthiophene) Grown by Directional Epitaxial Solidification.
Advanced Functional Materials, 17(1):101 (2007).
doi:10.1002/adfm.200600673.

[30] Kayunkid, N. *et al.*

Structural Model of Regioregular Poly(3-hexylthiophene) Obtained by Electron Diffraction Analysis.
Macromolecules, 43(11):4961 (2010).
doi:10.1021/ma100551m.

[31] Wu, Z. *et al.*
Temperature and Molecular Weight Dependent Hierarchical Equilibrium Structures in Semiconducting Poly(3-hexylthiophene).
Macromolecules, 43(10):4646 (2010).
doi:10.1021/ma902566h.

[32] Prosa, T. J. *et al.*
X-ray structural studies of poly(3-alkylthiophenes): an example of an inverse comb.
Macromolecules, 25(17):4364 (1992).
doi:10.1021/ma00043a019.

[33] Tashiro, K. *et al.*
Crystal structural change in poly(3-alkyl thiophene)s induced by iodine doping as studied by an organized combination of X-ray diffraction, infrared/Raman spectroscopy and computer simulation techniques.
Polymer, 38(12):2867 (1997).

[34] Logothetidis, S. and Laskarakis, a.
Towards the optimization of materials and processes for flexible organic electronics devices.
The European Physical Journal Applied Physics, 46(1):12502 (2009).
doi:10.1051/epjap/2009041.

[35] Ohkita, H. *et al.*
Charge carrier formation in polythiophene/fullerene blend films studied by transient absorption spectroscopy.
Journal of the American Chemical Society, 130(10):3030 (2008).
doi:10.1021/ja076568q.

[36] Hummelen, J. *et al.*
Preparation and characterization of fulleroid and methanofullerene derivatives.
J. Org. Chem., 60(3):532 (1995).
doi:10.1021/jo00108a012.

[37] Sariciftci, N. S. *et al.*
Photoinduced electron transfer from a conducting polymer to buckminsterfullerene.

Science (New York, N.Y.), 258(5087):1474 (1992).
doi:10.1126/science.258.5087.1474.

[38] Kanai, Y. and Grossman, J. C.
Insights on interfacial charge transfer across P3HT/fullerene photovoltaic heterojunction from Ab initio calculations.
Nano letters, 7(7):1967 (2007).
doi:10.1021/nl0707095.

[39] Piris, J. *et al.*
Photogeneration and Ultrafast Dynamics of Excitons and Charges in P3HT/PCBM Blends.
The Journal of Physical Chemistry C, 113(32):14500 (2009).
doi:10.1021/jp904229q.

[40] Hoppe, H. and Sariciftci, N. S.
Morphology of polymer/fullerene bulk heterojunction solar cells.
Journal of Materials Chemistry, 16(1):45 (2006).
doi:10.1039/b510618b.

[41] Martens, T.
Disclosure of the nanostructure of MDMO-PPV:PCBM bulk hetero-junction organic solar cells by a combination of SPM and TEM.
Synthetic Metals, 138(1-2):243 (2003).
doi:10.1016/S0379-6779(02)01311-5.

[42] Yang, X. *et al.*
Crystalline organization of a methanofullerene as used for plastic solar-cell applications.
Advanced Materials, 16(910):802 (2004).
doi:10.1002/adma.200306372.

[43] Hoppe, H. *et al.*
Nano-Crystalline Fullerene Phases in Polymer/Fullerene Bulk-Heterojunction Solar Cells: A Transmission Electron Microscopy Study.
Synthetic Metals, 152(1-3):117 (2005).
doi:10.1016/j.synthmet.2005.07.217.

[44] Hayashi, Y. *et al.*
Investigation of Pcbm Concentration on Photovoltaic Characteristics of Polymer Solar Cells with Blends of P3Ht and Pcbm.
2006 IEEE 4th World Conference on Photovoltaic Energy Conference, pages 271–274 (2006).

doi:10.1109/WCPEC.2006.279443.

[45] Kim, J. Y. and Frisbie, C. D.
Correlation of Phase Behavior and Charge Transport in Conjugated Polymer/Fullerene Blends.
Journal of Physical Chemistry C, 112(45):17726 (2008).
doi:10.1021/jp8061493.

[46] Chiu, M.-Y. *et al.*
Morphologies of Self-Organizing Regioregular Conjugated Polymer/Fullerene Aggregates in Thin Film Solar Cells.
Macromolecules, 43(1):428 (2010).
doi:10.1021/ma901895d.

[47] Erb, T. *et al.*
Correlation Between Structural and Optical Properties of Composite Polymer/Fullerene Films for Organic Solar Cells.
Advanced Functional Materials, 15(7):1193 (2005).
doi:10.1002/adfm.200400521.

[48] Reyes-Reyes, M. *et al.*
Methanofullerene elongated nanostructure formation for enhanced organic solar cells.
Thin Solid Films, 516(1):52 (2007).
doi:10.1016/j.tsf.2007.04.166.

[49] Woo, C. H. *et al.*
The influence of poly(3-hexylthiophene) regioregularity on fullerene-composite solar cell performance.
Journal of the American Chemical Society, 130(48):16324 (2008).
doi:10.1021/ja806493n.

[50] Wang, W. *et al.*
High-efficiency polymer photovoltaic devices from regioregular-poly(3-hexylthiophene-2,5-diyl) and [6,6]-phenyl-C[sub 61]-butyric acid methyl ester processed with oleic acid surfactant.
Applied Physics Letters, 90(18):183512 (2007).
doi:10.1063/1.2735937.

[51] Bulle-Lieuwma, C.
Characterization of polymer solar cells by TOF-SIMS depth profiling.
Applied Surface Science, 203-204:547 (2003).
doi:10.1016/S0169-4332(02)00756-0.

[52] Rispens, M. T. *et al.*
Influence of the solvent on the crystal structure of PCBM and the efficiency of MDMO-PPV:PCBM 'plastic' solar cells.
Chemical communications, pages 2116–2118 (2003).

[53] Huang, J.-S. *et al.*
Enhancing performance of organic–inorganic hybrid solar cells using a fullerene interlayer from all-solution processing.
Solar Energy Materials and Solar Cells, 94(2):182 (2010).
doi:10.1016/j.solmat.2009.08.019.

[54] Kim, Y. *et al.*
Distorted asymmetric cubic nanostructure of soluble fullerene crystals in efficient polymer:fullerene solar cells.
ACS nano, 3(9):2557 (2009).
doi:10.1021/nn900798m.

[55] Ecija, D. *et al.*
Crossover site-selectivity in the adsorption of the fullerene derivative PCBM on Au(111).
Angewandte Chemie (International ed. in English), 46(41):7874 (2007).
doi:10.1002/anie.200702531.

[56] Li, L. *et al.*
Epitaxy-Assisted Creation of PCBM Nanocrystals and Its Application in Constructing Optimized Morphology for Bulk-Heterojunction Polymer Solar Cells.
J. Phys. Chem. B, 112:15651 (2008).

[57] Dabirian, R. *et al.*
Micron-sized [6,6]-phenyl C61 butyric acid methyl ester crystals grown by dip coating in solvent vapour atmosphere: interfaces for organic photovoltaics.
Physical chemistry chemical physics : PCCP, 12(17):4473 (2010).
doi:10.1039/b923496a.

[58] Kronenberg, N. *et al.*
Tailored merocyanine dyes for solution-processed BHJ solar cells.
Journal of Materials, 20(2):240 (2010).
doi:10.1039/b916181c.

[59] Zeng, L. *et al.*
Modulation of Phase Separation Between Spherical and Rodlike Molecules Using Geometric Surfactancy.

Langmuir : the ACS journal of surfaces and colloids, (Xx) (2010).
doi:10.1021/la1014797.

[60] Hahn, T., editor.
International Tables for Crystallography, volume A of *International Tables for Crystallography*.
International Union of Crystallography, Chester, England (2006).
ISBN 978-0-7923-6590-7.
doi:10.1107/97809553602060000100.

[61] Landau, L. D. *et al.*
Statistical physics, Part 1.
Butterworth-Heinemann (1980).
ISBN 0750633727.

[62] Görling, A.
Density-functional theory for excited states.
Physical Review A, 54(5):3912 (1996).
doi:10.1103/PhysRevA.54.3912.

[63] Durand, P. and Barthelat, J.-C.
A theoretical method to determine atomic pseudopotentials for electronic structure calculations of molecules and solids.
Theoretica Chimica Acta, 38(4):283 (1975).
doi:10.1007/BF00963468.

[64] Barthelat, J. *et al.*
Non-empirical pseudopotentials for molecular calculations.
Molecular Physics, 33(1):159 (1977).
doi:10.1080/00268977700103141.

[65] Becke, A.
Density-functional exchange-energy approximation with correct asymptotic behavior.
Physical Review A (1988).

[66] Lee, C. *et al.*
Development of the Colle-Salvetti correlation-energy formula into a functional of the electron density.
Physical Review B, 37(2):785 (1988).

[67] Sprik, M. *et al.*
Ab initio molecular dynamics simulation of liquid water: Comparison of three gradient-corrected density functionals.

The Journal of Chemical Physics, 105(3):1142 (1996).
doi:10.1063/1.471957.

[68] Belonoshko, a. B. and Rosengren, a.
Ab Initio Study of Water Interaction with a Cu Surface (dagger).
Langmuir : the ACS journal of surfaces and colloids, 108(3) (2010).
doi:10.1021/la101374r.

[69] Kohanoff, J.
Electronic structure calculations for solids and molecules.
Cambridge University Press (2006).

Acronyms

AFM atomic force microscopy.

BCC body centered cubic.

BHJ bulk heterojunction.

CB chlorobenzene.

CGS copper gallium diselenide.

CIGS copper indium gallium diselenide.

CIS copper indium diselenide.

CN-MEH-PPV poly-(2-methoxy-5-(2'-ethylhexyloxy)).

CPV concentrating photovoltaics.

DFT density functional theory.

EQE external quantum efficiency.

FCC face centered cubic.

FF fill factor.

HOMO highest occupied molecular orbital.

HT head to tail.

IR infrared.

KS Kohn-Sham.

LUMO lowest unoccupied molecular orbital.

MDMO-PPV poly-(2-methoxy-5-(3,7-dimethyloctyloxy))-1,4-phenylene-vinylene.

MO molecular orbital.

MW molecular weight.

ODCB ortho-dichlorobenzene.

OSC organic solar cell.

P3AT poly-(3 alkylthiophene).

P3HT poly-(3 hexylthiophene).

PAT poly-acetylene.

PCBM phenyl-C_{61}-butyric acid methyl ester.

PCE power conversion efficiency.

PPV poly-phenylene-vinylene.

PR photoresponsivity.

PSC polymer solar cell.

PT poly-thiophene.

PV photovoltaic.

QM quantum mechanic.

SAED selected area electron diffraction.

SCF self consistent field.

SCU simple cubic.

TEM transmission electron microscopy.

UV ultraviolet.

XRD x-ray diffraction.